

This is a repository copy of *Ancestral Admixture Is the Main Determinant of Global Biodiversity in Fission Yeast*.

White Rose Research Online URL for this paper:  
<https://eprints.whiterose.ac.uk/148837/>

Version: Accepted Version

---

**Article:**

Tusso, Sergio, Nieuwenhuis, Bart P S, Sedlazeck, Fritz J et al. (3 more authors) (2019) *Ancestral Admixture Is the Main Determinant of Global Biodiversity in Fission Yeast*. *Molecular Biology and Evolution*. 1975–1989. ISSN 0737-4038

<https://doi.org/10.1093/molbev/msz126>

---

**Reuse**

Items deposited in White Rose Research Online are protected by copyright, with all rights reserved unless indicated otherwise. They may be downloaded and/or printed for private study, or other acts as permitted by national copyright laws. The publisher or other rights holders may allow further reproduction and re-use of the full text version. This is indicated by the licence information on the White Rose Research Online record for the item.

**Takedown**

If you consider content in White Rose Research Online to be in breach of UK law, please notify us by emailing [eprints@whiterose.ac.uk](mailto:eprints@whiterose.ac.uk) including the URL of the record and the reason for the withdrawal request.

**Ancestral admixture is the main determinant of global biodiversity in fission yeast**

Sergio Tusso <sup>1,2,\*</sup>, Bart P.S. Nieuwenhuis <sup>1</sup>, Fritz J. Sedlazeck <sup>3</sup>, John W. Davey <sup>4</sup>, Daniel C. Jeffares <sup>5,6</sup>, Jochen B. W. Wolf<sup>1,2,\*</sup>

<sup>1</sup> Division of Evolutionary Biology, Faculty of Biology, LMU Munich, Grosshaderner Str. 2, 82152 Planegg-Martinsried, Germany

<sup>2</sup> Science for Life Laboratories and Department of Evolutionary Biology, Norbyvägen 18D, 75236 Uppsala University, 75236 Uppsala, Sweden

<sup>3</sup> Human Genome Sequencing Center, Baylor College of Medicine, One Baylor Plaza, Houston TX 77030

<sup>4</sup> Bioscience Technology Facility, Department of Biology, University of York, Wentworth Way, York YO10 5DD, United Kingdom

<sup>5</sup> Department of Biology, University of York, Wentworth Way, York YO10 5DD, United Kingdom

<sup>6</sup> York Biomedical Research Institute (YBRI), University of York, Wentworth Way, York YO10 5DD, United Kingdom

\* Authors to whom correspondence should be addressed

**Corresponding authors:**

Sergio Tusso: [situssog@gmail.com](mailto:situssog@gmail.com)

Jochen B. W. Wolf: [j.wolf@biologie.uni-muenchen.de](mailto:j.wolf@biologie.uni-muenchen.de)

36 **Mutation and recombination are key evolutionary processes governing phenotypic variation and**  
37 **reproductive isolation. We here demonstrate that biodiversity within all globally known strains**  
38 **of *Schizosaccharomyces pombe* arose through admixture between two divergent ancestral**  
39 **lineages. Initial hybridization was inferred to have occurred ~20-60 sexual outcrossing**  
40 **generations ago consistent with recent, human-induced migration at the onset of intensified**  
41 **transcontinental trade. Species-wide heritable phenotypic variation was explained near-**  
42 **exclusively by strain-specific arrangements of alternating ancestry components with evidence for**  
43 **transgressive segregation. Reproductive compatibility between strains was likewise predicted by**  
44 **the degree of shared ancestry. To assess the genetic determinants of ancestry block distribution**  
45 **across the genome, we characterized the type, frequency and position of structural genomic**  
46 **variation (SV) using nanopore and single-molecule real time sequencing. Despite being**  
47 **associated with double-strand break initiation points, over 800 segregating structural variants**  
48 **exerted overall little influence on the introgression landscape or on reproductive compatibility**  
49 **between strains. In contrast, we found strongly increased statistical linkage between ancestral**  
50 **populations consistent with negative epistatic selection shaping genomic ancestry combinations**  
51 **during the course of hybridization. This study provides a detailed, experimentally tractable**  
52 **example that genomes of natural populations are mosaics reflecting different evolutionary**  
53 **histories. Exploiting genome-wide heterogeneity in the history of ancestral recombination and**  
54 **lineage-specific mutations sheds new light on the population history of *S. pombe* and highlights**  
55 **the importance of hybridization as a creative force in generating biodiversity.**

56  
57

## 58 **Introduction**

59 Mutation is the ultimate source of biodiversity. In sexually reproducing organisms it is assisted by  
60 recombination shuffling mutations of independent genomic backgrounds into millions of novel  
61 combinations. This widens the phenotypic space upon which selection can act and thereby accelerates  
62 evolutionary change (Muller, 1932; Fisher, 1999; McDonald et al., 2016). This effect is enhanced for  
63 heterospecific recombination between genomes of divergent populations (Abbott et al., 2013). Novel  
64 combinations of independently accumulated mutations can significantly increase the overall genetic  
65 and phenotypic variation, even beyond the phenotypic space of parental lineages (transgressive  
66 segregation (Lamichhaney et al., 2017; Nolte and Sheets, 2005)). Yet, if mutations of the parental  
67 genomes are not compatible to produce viable and fertile offspring, hybridization is a dead end.  
68 Phenotypic variation then remains within the confines of genetic variation of each reproductively  
69 isolated, parental lineage.

70

71 It is increasingly recognised that hybridization is commonplace in nature, and constitutes an important  
72 driver of diversification (Abbott et al., 2013; Mallet, 2005). Ancestry components of hybrid genomes

73 can range from clear dominance of alleles from the more abundant species (Dowling et al., 1989;  
74 Taylor and Hebert, 1993), over a range of admixture proportions (Lamichhaney et al., 2017;  
75 Runemark et al., 2018) to the transfer of single adaptive loci (The Heliconius Genome Consortium et  
76 al., 2012). The final genomic composition is determined by a complex interplay of demographic  
77 processes, heterogeneity in recombination (e.g. induced by genomic rearrangements) (Wellenreuther  
78 and Bernatchez, 2018) and selection (Sankararaman et al., 2014; Schumer et al., 2016). Progress in  
79 sequencing technology, now allows characterisation of patterns of admixture and the illumination of  
80 underlying processes (Payseur and Rieseberg, 2016). Yet, research has largely focused on animals  
81 (Turner and Harr, 2014; Vijay et al., 2016; Meier et al., 2017; Jay et al., 2018) and plants (Twyford et  
82 al., 2015) and relatively little attention has been paid to natural populations of sexually reproducing  
83 micro-organisms (Leducq et al., 2016; Stukenbrock, 2016; Peter et al., 2018; Steenkamp et al., 2018).

84  
85 The fission yeast *Schizosaccharomyces pombe* is an archiascomycete haploid unicellular fungus with a  
86 facultative sexual mode of reproduction. Despite of its outstanding importance as a model system in  
87 cellular biology (Hoffman et al., 2015) and the existence of global sample collections, essentially all  
88 research has been limited to a single isogenic strain isolated by Leupold in 1949 (Leupold 972; JB22  
89 in this study). Very little is known about the ecology, origin, and evolutionary history of the species  
90 (Jeffares, 2018). Global population structure has been described as shallow with no apparent  
91 geographic stratification (Jeffares et al., 2015). Genetic diversity ( $\pi = 3 \cdot 10^{-3}$  substitutions/site) appears  
92 to be strongly influenced by genome-wide purifying selection with the possible exception of region-  
93 specific balancing selection (Fawcett et al., 2014; Jeffares et al., 2015). Despite the overall low genetic  
94 diversity, *S. pombe* shows abundant additive genetic variation in a variety of phenotypic traits  
95 including growth, stress responses, cell morphology, and cellular biochemistry (Jeffares et al., 2015).  
96 The apparent worldwide lack of genetic structure in this species appears inconsistent with the large  
97 phenotypic variation between strains and with evidence for post-zygotic reproductive isolation  
98 between inter-strain crosses, ranging from 1% to 90 % of spore viability (Kondrat'eva and Naumov,  
99 2001; Teresa Avelar et al., 2013; Zanders et al., 2014; Jeffares et al., 2015; Naumov et al., 2015;  
100 Marsellach, 2017).

101  
102 In this study, we integrate whole-genome sequencing data from three different technologies -  
103 sequencing-by-synthesis (Illumina technology data accessed from (Jeffares et al., 2015)), single-  
104 molecule real-time sequencing (Pacific BioSciences technology, this study) and nanopore sequencing  
105 (Oxford Nanopore technology, this study) - sourced from a mostly human-associated, global sample  
106 collection to elucidate the evolutionary history of the *S. pombe* complex. Using population genetic  
107 analyses based on single nucleotide polymorphism (SNP) we show that global genetic variation and  
108 heritable phenotype variation of *S. pombe* results from recent hybridization of two ancient lineages. 25  
109 *de novo* assemblies from 17 divergent strains further allowed us to quantify segregating structural

110 variation including insertions, deletions, inversion and translocations. In light of these findings, we  
111 retrace the global population history of the species, and discuss the relative importance of genome-  
112 wide ancestry and structural mutations in explaining phenotypic variation and reproductive isolation.

113

## 114 **Results**

115

### 116 **Global genetic variation in *S. pombe* is characterized by ancient admixture**

117 Genetic variation of the global *S. pombe* collection comprises 172,935 SNPs segregating in 161 strains.

118 Considering SNPs independently, individuals can be sub-structured into 57 clades that differ by more  
119 than 1900 variants, but are near-clonal within clades (Jeffares et al., 2015). To examine population

120 ancestry further, we divided the genome into 1925 overlapping windows containing 200 SNPs each

121 and selected one representative from each clade (57 samples in total). Principle component analysis

122 conducted on each orthologous window showed a highly consistent pattern along the genome (**Figure**

123 **1a, Supplementary Figure 1**): i) the major axis of variation (PC1) split all samples into two clear

124 discrete groups explaining  $60\% \pm 13\%$  of genetic variance (**Figure 1b**). ii) All samples fell into either

125 extreme of the normalized distribution of PC1 scores ( $PC1 \in [0; 0.25] \cup [0.75; 1]$ )

126 (**Supplementary Figures 2 & 3**) with the only exception of strains with inferred changes in ploidy

127 level (**Methods, Supplementary Figure 4**). iii) PC2 explained  $13\% \pm 6\%$  of variation and

128 consistently attributed higher variation to one of the two groups. This strong signal of genomic

129 windows separating into two discrete groups suggested that the genomic diversity in this collection

130 was derived from two distinct ancestral populations. However, iv) group membership of strains

131 changes among windows moving along the genome, reflecting recombination between these two well

132 defined groups. Forwards population simulations followed by principle component analysis with SNP

133 windows showed that this signal was unlikely to be an artefact (see **Methods**). This last point

134 highlights the importance of considering haplotype structure and explains the lack of observed

135 population structure when disregarding non-independence of SNPs (Jeffares et al., 2015).

136

137 The strong signal from the PCA systematically differentiating groups along the genome was likewise

138 reflected in population genetic summary statistics including Watterson's theta ( $\theta$ ), pairwise nucleotide

139 diversity ( $\pi$ ), and Tajima's D (**Figure 1d and 2**). Significant differences in these statistics (Kendall's  $\tau$

140  $p\text{-value} \leq 2.2 \cdot 10^{-16}$ ) were also present in mitochondrial genetic variation (**Figure 1a**) and allowed

141 polarising the two groups across windows into a 'low-diversity' group (red) and a 'high-diversity group

142 (blue) (**Figure 1a, Supplementary Figure 5**). Genetic divergence between groups ( $D_{xy}$ ) was 15 and 3

143 times higher than mean genetic diversity ( $\pi$ ) within each group, respectively, and thus supports a

144 period of independent evolution. Painting genomic windows by group membership revealed blocks of

145 ancestry distributed in sample specific patterns along the genome (**Figure 1c, Supplementary Figure**

146 **6**). The sample corresponding to the reference genome isolated originally from Europe (Leupold's

147 972; JB22) consisted almost exclusively of 'red' ancestry (>96% red), whereas other samples were  
148 characterized near-exclusively by 'blue' ancestry (>96% blue). The sample considered to be a different  
149 species from Asia, *S. kambucha* (JB1180 (Singh and Klar, 2002)) had a large proportion of 'blue'  
150 windows (>70% blue). Hereafter, we refer to the 'red' and 'blue' clade as *Sp* and *Sk*, for *S. pombe* and *S.*  
151 *kambucha* respectively.

152

153 Next, we explored different historical processes that may underlie the deep divergence between these  
154 clades and their distribution along the genome. Using individual based forward simulations we  
155 contrasted a historical scenario of divergence in allopatry followed by extensive, recent hybridization  
156 with a scenario of low, but constant levels of gene flow during divergence. The empirical level of  
157 divergence between ancestral groups in combination with the observed distribution of recombinant  
158 block size along the genome could not be recovered under a demographic model of divergence with  
159 constant gene flow. The simulations much rather provide support for a scenario of divergence in  
160 isolation followed by a recent pulse of gene flow recovering both ancestral divergence and the  
161 observed introgression landscape (see Material and Methods, **Supplementary Figures 7 and 8**).

162

163 The distribution of ancestry components was highly heterogeneous across the chromosome (**Figure**  
164 **2a**). Most strains showed an excess of *Sp* ancestry in parts of chromosome I, whereas several regions  
165 of chromosome III had an excess of *Sk* ancestry. Grouping samples by the pattern of genomic ancestry  
166 across the genome revealed eight discrete consistent clusters (**Figure 1c**). Consistent with independent  
167 and/or recent segregation of ancestral groups, cluster membership for several samples differed  
168 between chromosomes (**Figure 1c**) and genome components (**Supplementary Figures 9 & 10**). This  
169 is also reflected by low support in the relationship between the eight clusters. Failing to incorporate  
170 this genome-wide variation of admixture proportions can mimic signatures of selection. For example,  
171 equal ancestry contributions for a certain genomic region will yield high positive values of both  
172 Tajima's D (**Supplementary Figure 11**) and  $\pi$  and may be mistaken as evidence for balancing  
173 selection. Strong skew in ancestry proportions reduces both statistics to values of the prevailing  
174 ancestry and may appear as evidence for selective sweeps (**Figure 2b**). Taking ancestry into account,  
175 however, there was no clear signature of selection in either *Sp* or *Sk* genetic variation that could  
176 account for heterogeneity in the genetic composition of hybrids (**Supplementary Figure 11**).  
177 Signatures of selection identified previously (cf. Fawcett et al., 2014) are likely artefacts due to  
178 skewed ancestry proportions rather than events of positive or balancing selection in the ancestral  
179 populations.

180

181 Overall, our results provide strong evidence for the presence of at least two divergent ancestral  
182 populations: one genetically diverse group (*Sk* clade) and a less diverse group (*Sp* clade). We found a  
183 large range of ancestral admixture proportions between these two clades broadly clustering samples

184 into 8 weakly supported groups. These resemble clusters of strains previously identified by *Structure*  
185 and *fineStructure* without explicit modelling of ancestral admixture (Jeffares et al., 2015). Neglecting  
186 ancestry, Jeffares et al. (2015) argued that the shallow population structure likely results from  
187 extensive gene flow between clusters. Yet, considering the genome-wide distribution of discrete *Sk*  
188 and *Sp* ancestry, and lack of geographical structure, suggests that the 8 clusters are derived from one or  
189 a few centres of ancient admixture (hybridization) without having to invoke subsequent or recent gene  
190 flow between them.

191

### 192 **Age of ancestral lineages and timing of hybridization**

193 To shed further light on the population history, we estimated the age of the parental lineages and the  
194 timing of initial hybridization. Calibrating mitochondrial divergence by known collection dates over  
195 the last 100 years, Jeffares et al. (2015) estimated that the time to the most recent common ancestor for  
196 all samples was around 2,300 years ago. Current overrepresentation of near-pure *Sp* and *Sk* in Europe  
197 or Africa / Asia, respectively, is consistent with an independent history of the parental lineages on  
198 different continents for the most part of the last millennia (**Supplementary Figure 10**). Yet, the  
199 variety of admixed genomes bears testimony to the fact that isolation has been disrupted by  
200 heterospecific gene flow. Using a theoretical model assuming secondary contact with subsequent  
201 hybridization (Janzen et al., 2018) as supported by the data, we estimated that hybridization occurred  
202 within the last around 20 to 60 sexual outcrossing generations depending on window size (**Figure 3**,  
203 **Supplementary Figures 12 & 13**). Considering intermittent generations of asexual reproduction, high  
204 rates of haploid selfing and dormancy of spores (Farlow et al., 2015; Jeffares, 2018) it is difficult to  
205 obtain a reliable estimate of time in years. Yet, the range of estimates of hybridization timing is  
206 consistent with hybridization induced by the onset of regular trans-continental human trade between  
207 Europe with Africa and Asia (~14th century) and with the Americas (~16th century), with fission  
208 yeast as a human commensal (Jeffares, 2018). This fits with the observation that all current samples  
209 from the Americas were hybrids, while samples with the purest ancestry stem from Europe, Africa and  
210 Asia. Moreover, negative genome-wide Tajima's D estimates for both ancestral clades (mean  $\pm$  SD for  
211 *Sp*:  $-0.8 \pm 0.9$  and *Sk*:  $-0.7 \pm 0.6$ ) signal a period of recent expansion.

212

### 213 **Heritable phenotypic variation and reproductive isolation are governed by ancestry components**

214 Hybridization can lead to rapid evolution due to selection acting on the genetic and phenotypic  
215 variation emerging after admixture (Muller, 1932; Fisher, 1999; McDonald et al., 2016). We assessed  
216 the consequences of hybridization on phenotypic variation making use of a large data set including  
217 228 quantitative traits collected from the strains under consideration here (Jeffares et al., 2015).  
218 Contrary to genetic clustering of hybrid genomes (**Figure 1c**), samples with similar ancestry  
219 proportions did not group in phenotypic space described by the first two PC-dimensions capturing  
220 31% of the total variance across traits (**Figure 4a**). Moreover, phenotypic variation of hybrids

221 exceeded variation of pure strains ( $>0.9$  ancestry for *Sp* or *Sk*). This was supported by trait specific  
222 analyses. We divided samples into three discrete groups: pure *Sp*, pure *Sk* and hybrids with a large  
223 range of *Sp* admixture proportions (0.1-0.9). 63 traits showed significant difference among groups  
224 (**Figure 4b, Supplementary Figure 14**). In the vast majority of cases (50 traits), hybrid phenotypes  
225 were indistinguishable from one of the parents, but differed from the other, suggesting dominance of  
226 one ancestral background, consistent with some ecological separation of the backgrounds. In seven  
227 traits, hybrid phenotypes were intermediate differing from both parents, consistent with an additive or  
228 polygenic contribution of both ancestral backgrounds. For six traits, hybrids exceeded phenotypic  
229 values of both parents providing evidence for transgressive segregation. In all cases, the number of  
230 significantly differentiated traits was found to be higher than under the null model (mean number of  
231 significant traits after 10000 permutations: dominant *Sk*  $4 \pm 2$ , dominant *Sp*  $4 \pm 2$ , transgressive  $0$   
232  $\pm 0.3$ , intermediate  $0 \pm 0.1$ ; **Supplementary Figure 15**). Jeffares et al. (2017) showed that for each  
233 trait the total proportion of phenotypic variance explained by the additive genetic variance component  
234 (used as an estimated of the narrow-sense heritability) ranged from 0 to around 90%. We found that  
235 across all 228 traits, considering *Sp* and *Sk* ancestry components across the 1,925 genomic windows  
236 explained an equivalent amount of phenotypic variance as all 172,935 SNPs segregating across all  
237 samples, being both highly correlated (**Figure 4c, 4d**;  $r = 0.82$ ,  $p\text{-value} \leq 2.2 \cdot 10^{-16}$ ). Combinations of  
238 ancestral genetic variation appear to be the main determinants of heritable phenotypic variation with  
239 only little contribution from single-nucleotide mutations arising after admixture. In turn, this supports  
240 that the formation of hybrids is recent (see above), and few (adaptive) mutations have occurred after it.

241  
242 Ancestry also explained most of the variation in postzygotic reproductive isolation between strains.  
243 Previous work revealed a negative correlation between spore viability and genome-wide SNP  
244 divergence between strains (Jeffares et al., 2015). The degree of similarity in genome-wide ancestry  
245 had the same effect: the more dissimilar two strains were in their ancestry, the lower the viability of  
246 the resulting spores (**Figure 4e**; Kendall correlation coefficients,  $\tau = -0.30$ ,  $T = 259$ ,  $p\text{-value} =$   
247  $6.66 \cdot 10^{-3}$ ). This finding is consistent with reproductive isolation being governed by many, genome-  
248 wide incompatibilities between the *Sp* and *Sk* clade. Yet, in a number of cases spore survival was  
249 strongly reduced in strain combinations with near-identical ancestry. In these cases, reproductive  
250 isolation may be caused by few large effect mutations, including structural genomic changes that arose  
251 after hybridization.

252

### 253 **Structural mutations do not determine the genome-wide distribution of ancestry blocks**

254 Structural genomic changes (structural variants or SVs hereafter) are candidates for large-effect  
255 mutations governing phenotypic variation (Küpper et al., 2016; Jeffares et al., 2017), reproductive  
256 isolation (Hoffmann and Rieseberg, 2008; Teresa Avelar et al., 2013) and heterospecific  
257 recombination (Ortiz-Barrientos et al., 2016). They may thus importantly contribute to shaping



258 heterogeneity in the distribution of ancestry blocks observed along the genome (Jay et al., 2018;  
259 Poelstra et al., 2014) (**Figure 2b**). However, inference of SVs in natural strains of fission yeast has  
260 been primarily based on short-read sequencing (Jeffares et al., 2017). SV calls from short-read  
261 sequencing data are known to differ strongly by bioinformatic pipeline, are prone to false positive  
262 inference and are limited in their ability to infer long-range SVs, in particular in repetitive regions of  
263 the genome (Jeffares et al., 2017).

264

265 To obtain a reliable and comprehensive account of SVs segregating across strains and test for a  
266 possible association of SVs with the skewed ancestry in the genome, we generated chromosome-level  
267 *de novo* genome assemblies for 17 of the most divergent samples using single-molecule real time  
268 sequencing (mean sequence coverage 105x; **Supplementary Table 7**). For the purpose of  
269 methodological comparison, we also generated *de novo* assemblies for a subset of 8 strains (including  
270 the reference Leupold's 972) based on nanopore sequencing (mean sequence coverage: 140x). SVs  
271 were called using a mixed approach combining alignment of *de novo* genomes and mapping of  
272 individual reads to the reference genome (Wood et al., 2002). Both approaches and technologies  
273 yielded highly comparable results (**Methods, Supplementary Figure 16-19 and Supplementary**  
274 **Table 8**).

275

276 After quality filtering, we retained a total of 832 variant calls including 563 insertions or deletions  
277 (indels), 118 inversions, 110 translocations and 41 duplications. The 17 strains we examined with long  
278 reads could be classified into six main karyotype arrangements (**Figure 5a**). The previously reported  
279 list of SVs of the same strains using short reads consisted of only 52 SVs (Jeffares et al., 2017) of  
280 which only 8 were found to overlap with the 832 calls from long-read data. The vast majority of SVs  
281 were smaller than 10 kb (**Figure 5b**). The size distribution was dominated by elements of 6 kb and 0.5  
282 kb in length corresponding to known transposable elements (TEs) and their flanking long terminal  
283 regions (LTRs), respectively (Kelly and Levin, 2005). Only a small number of SVs corresponded to  
284 large-scale rearrangements (50 kb - 2.2 Mb) including translocations between chromosomes (**Figure**  
285 **5a**). A subset of these have been characterized previously as large-effect modifiers of recombination  
286 promoting reproductive isolation (Brown et al., 2011; Teresa Avelar et al., 2013; Jeffares et al., 2017).

287

288 Contrary to previous SV classification based on short reads (Jeffares et al., 2017), SV density was not  
289 consistently increased in repetitive sequences such as centromeric and telomeric regions illustrating  
290 the difficulty of short-read data in resolving SVs in repetitive regions (**Figure 5c**). Instead, we found  
291 that the frequency of SVs was significantly elevated in close proximity to developmentally  
292 programmed DNA double-strand breaks (DSB) associated with recombination initiation (Fowler et al.,  
293 2014). The proportion of SVs observed within [0, 0.5) kb and [0.5, 1) kb of DSB was increased by  
294 46% (p-value <  $1 \cdot 10^{-4}$ ) and 67% (p-value <  $1 \cdot 10^{-4}$ ) relative to random expectations. On the contrary,

295 regions more distant than 10 kb from DSB were relatively depleted of SVs (**Supplementary Figure**  
296 **20**).

297

298 Next, we imputed the ancestry of SV alleles from SNPs surrounding SV break points. We calculated  
299 allele frequencies for SVs in both ancestral clades and constructed a folded two-dimensional site  
300 frequency spectrum (**Figure 5d**). The majority of variants (66 %) segregated at frequencies below 0.3  
301 in both ancestral genetic backgrounds. Very few SVs were differentiated between ancestral  
302 populations (3 % of variants with frequency higher than 0.9 in one population and below 0.1 in the  
303 other). This pattern contrasted with the reference spectrum derived from SNPs where the proportion of  
304 low frequency variants was similar at 60 %, but genetic differentiation between populations was  
305 substantially higher (21 % of SNP variants with frequency higher than 0.9 in one population and  
306 below 0.1 in the other). The difference was most pronounced for large SVs (larger than 10 kb) and  
307 TEs, for which we estimated allele frequencies for all 57 strains by means of PCR and short-read data,  
308 respectively. For TE's, 98 % of the total 1048 LTR variants segregated at frequencies below 0.3 in  
309 both ancestral populations without a single variant differentiating ancestral populations (**Figure 5d**).  
310 Large SVs likewise segregated at low frequencies, being present at most in two strains out of 57. This  
311 included the translocation reported for *S. kambucha* between chromosome II and III (Zanders et al.,  
312 2014), which we found to be specific for that strain. Only the large inversion on chromosome I  
313 segregated at higher frequency being present in five strains out of 57, of which three were of pure *Sp*  
314 ancestry including the reference strain (**Supplementary Table 10**). Additionally, SVs segregating at  
315 high frequency ( $> 0.7$ ) did not cluster in genomic regions with steep transitions in ancestry between *Sp*  
316 and *Sk* ancestry (large changes in ancestral frequency in **Figure 2a**.  $p$ -value  $> 0.1$ ; **Supplementary**  
317 **Figure 21**).

318

319 In summary, long-read sequencing provided a detailed account of species-wide diversity in structural  
320 genetic variation including over 800 high-quality variants ranging from small indels to large-scale  
321 inter-chromosomal rearrangements. SV calls showed substantial overlap among technologies (Pacific  
322 Biosciences, Nanopore) and approaches (de novo assembly vs. mapping), but less than 1 % of this  
323 variation was inferred from short-read data. This finding admonishes to caution when interpreting SV  
324 calls from short read data which are moreover sensitive to genotyping methods. In contrast to genome-  
325 wide SNPs, SVs segregated near-exclusively at low frequencies and were rarely differentiated by  
326 ancestral origin. This is consistent with strong diversity-reducing purifying selection relative to SNPs.  
327 The fact that SVs, including large-scale rearrangements with known effects on recombination and  
328 reproductive isolation (Brown et al., 2011; Teresa Avelar et al., 2013; Zanders et al., 2014), were often  
329 unique to single strains precludes a role of SVs in shaping patterns of ancestral heterospecific  
330 recombination. Moreover, while being concentrated in proximity to double-strand breaks, possibly due  
331 to improper repair upon recombination (Currall et al., 2013), SVs were not significantly associated

332 with steep transitions in ancestry blocks. Summarizing the evidence, SVs appear to have had limited  
333 influence in shaping genome-wide patterns of ancestral admixture. While they may reduce fitness of  
334 hybrids between specific strains, SV cannot explain the prevalence of reproductive isolation as a  
335 function on ancestral similarity (**Figure 4e**).

336

### 337 **Negative epistasis and the distribution of ancestral blocks**

338 Alternatively, heterogeneity in the distribution and frequency of ancestry along the genome may result  
339 from negative epistatic interactions of incompatible genetic backgrounds (Schumer et al., 2016). An  
340 excess of homospecific combinations of physically distant loci can serve as an indication of epistatic  
341 selection against genetic incompatibilities which can be segregating at appreciable frequencies even  
342 within species (Corbett-Detig et al., 2013). We tested this hypothesis by measuring ancestry  
343 disequilibrium (AD) between all possible pairs of genomic windows within a chromosome.  
344 Specifically, we quantified linkage disequilibrium (LD) between windows dominated by alleles from  
345 the same ancestral group ( $> 0.7$ ) *Sp-Sp* or *Sk-Sk* (reflecting positive AD) and contrasted it to the degree  
346 of linkage disequilibrium arising between heterospecific allele combinations *Sp-Sk* (negative AD)  
347 (**Supplementary Figure 22**). LD differed significantly between these two cases (**Figure 6**). While  
348 negative AD decreased rapidly with genetic distance ( $R^2 < 0.2$  after 66, 19 and 21 kb respectively for  
349 each chromosome) positive LD was higher in magnitude and extended over larger distances ( $R^2 < 0.2$   
350 after 1.02, 0.54, and 0.18 Mb respectively for each chromosome in *Sk-Sk* comparisons and 1.59, 1.12,  
351 and 0.32 Mb for *Sp-Sp* comparisons). This relationship remained significant after controlling for the  
352 potential effect of secondary population structure which can likewise increase apparent AD mimicking  
353 signatures of selection on epistatic genetic variation. Choosing only a single representative from each  
354 of the hybrid clusters (**Figure 1c**) LD remained larger for comparisons of genomic regions with the  
355 same ancestry. These results are overall consistent with a contribution of epistatic selection during the  
356 course of hybridization in shaping the ancestry composition of admixed genomes.

357

### 358 **Discussion**

359 This study adds to the increasing evidence that hybridization plays an important role as a rapid,  
360 'creative' evolutionary force in natural populations (Seehausen, 2004; Mallet, 2007; Soltis and Soltis,  
361 2009; Abbott et al., 2013; Schumer et al., 2014; Abbott et al., 2016; Pennisi, 2016; Nieto Feliner et al.,  
362 2017). Recent heterospecific recombination between two ancestral *S. pombe* populations shuffled  
363 genetic variation of genomes that diverged since classical antiquity about 2,300 years ago. With the  
364 necessary caution the timing of hybridization can be inferred to coincide with the onset of intensified  
365 trans-continental human trade, suggesting an anthropogenic contribution. Several samples showed  
366 similar distribution of ancestral blocks along the genome suggesting comparable evolutionary histories,  
367 and allowing the identification of 8 discrete clusters. These clusters, in general showed weak  
368 geographical grouping, initially interpreted as evidence for reduced population structure with large

369 recent world-wide gene flow (Jeffares et al., 2015). In contrast, the world-wide distribution of the two  
370 ancestral lineages suggests rapid and recent global dispersion after hybridization followed by local  
371 differentiation. This study thus highlights the importance of taking genomic non-independence into  
372 account. Allowing for the fact that genomes are mosaics reflecting different evolutionary histories can  
373 fundamentally alter inference on a species' evolutionary history.

374

375 Moreover, conceptualizing genetic variation as a function of ancestry blocks alternating along the  
376 genome changes the view on adaptation. Admixture is significantly faster than evolutionary change  
377 solely driven by mutation. Accordingly, phenotypic variation was near-exclusively explained by  
378 ancestry components with only little contribution from novel mutations. Importantly, admixture not  
379 only filled the phenotypic space between parental lineages, but also promoted transgressive  
380 segregation in several hybrids. This range of phenotypic outcomes opens the opportunity for hybrids  
381 to enter novel ecological niches (Nolte and Sheets, 2005; Pfennig et al., 2016) and track rapid  
382 environmental changes (Eroukhmanoff et al., 2013).

383

384 Structural mutations have been described as prime candidates for rapid large-effect changes with  
385 implications on phenotypic variation, recombination and reproductive isolation (Faria and Navarro,  
386 2010; Ortiz-Barrientos et al., 2016; Wellenreuther and Bernatchez, 2018). This study contributes to  
387 this debate providing a detailed account of over 800 high-quality structural variants identified across  
388 17 chromosome level *de novo* genomes sampled from the most divergent strains within the species.  
389 On the whole, SVs had little effect in our analysis. SVs segregated at low frequencies in both ancestral  
390 populations and, contrary to what has been suggested for specific genomic regions in other systems  
391 (Jay et al., 2018), they did not account for genome-wide heterogeneity in introgression among strains.  
392 Moreover, reproductive isolation was overall best predicted by the degree of shared ancestry with little  
393 contribution from SVs. Few crosses, however, showed strong reproductive isolation despite a high  
394 degree of shared ancestry (outliers in lower left corner of **Figure 4e**). In these cases, combining SVs  
395 from different strains into hybrid genomic backgrounds may have a significant impact. This is  
396 consistent with the observation that large, artificially generated rearrangements affect fitness (Teresa  
397 Avelar et al., 2013; Nieuwenhuis et al., 2018) and may promote reproductive isolation between  
398 specific *S. pombe* strains (Teresa Avelar et al., 2013; Zanders et al., 2014). Thus, reproductive  
399 isolation may arise by a combination of factors: negative epistasis between many loci with small to  
400 moderate effect differing in ancestry, and for specific strain combinations, single major effect  
401 (structural) mutations such as selfish elements or meiotic drivers (Zanders et al., 2014; Hu et al., 2017;  
402 Nuckolls et al., 2017). Functional work is needed to isolate these genetic elements.

403

404

405

406 **Material and Methods**

407

408 **Strains**

409 This study is based on a global collection of *S. pombe* consisting of 161 world-wide distributed strains  
410 (see **Supplementary Table 1**) described in Jeffares *et al.* (2015).

411

412 **Inferring ancestry components**

413 To characterize genetic variation across all strains, we made use of publically available data in variant  
414 call format (VCF) derived for all strains from Illumina sequencing with an average coverage of around  
415 80x (Jeffares *et al.*, 2015). The VCF file consists of 172,935 SNPs obtained after read mapping to the  
416 *S. pombe* 972 h<sup>-</sup> reference genome (ASM294v264) (Wood *et al.*, 2003) and quality filtering (see  
417 **Supplementary Table 1** for additional information). We used a custom script in R 3.4.3 (Team,  
418 2014) with the packages *gdsfmt* 1.14.1 and *SNPRelate* 1.12.2 (Zheng *et al.*, 2017, 2012), to divide the  
419 VCF file into genomic windows of 200 SNPs with overlap of 100 SNPs. This resulted in 1925  
420 genomic windows of 1 - 89 kb in length (mean 13 kb). For each window, we performed principal  
421 component analyses (PCA) using *SNPRelate* 1.12.2 (Zheng *et al.*, 2017, 2012) (example in **Figure 1a**  
422 and **Supplementary Figure 1**). The proportion of variance explained by the major axis of variation  
423 (PC1) was consistently high and allowed separating strains into two genetic groups/clusters, *Sp* and *Sk*  
424 (see main text, **Figure 1b**). Using individual based forward simulations with *SLiM* 3.2.1 (Haller and  
425 Messer, 2019) we found that this pattern cannot be obtained in the absence of population structure  
426 even for smaller window sizes including 5, 10, 20, 50 or 100 SNPs (**Supplementary Figures 23**).

427

428 We calculated population genetic parameters within clusters including pairwise nucleotide diversity  
429 ( $\pi$ ) (Nei and Li, 1979), Watterson theta ( $\theta_w$ ) (Watterson, 1975), and Tajima's *D* (Tajima, 1989), as  
430 well as the average number of pairwise differences between clusters ( $D_{xy}$ ) (Nei and Li, 1979) using  
431 custom scripts. Statistical significance of the difference in nucleotide diversity ( $\pi$ ) between ancestral  
432 clades was inferred using Kendall's  $\tau$  as test statistic. Since values of adjacent windows are  
433 statistically non-independent due to linkage, we randomly subsampled 200 windows along the genome  
434 with replacement. This was repeated a total of 10 times for each test statistic, and we report the  
435 maximum p-value. Given the consistent difference between clusters (**Figure 1** and **Supplementary**  
436 **Figure 2, 3 and 5**), normalised PC score could be used to attribute either *Sp* (low-diversity) or *Sk*  
437 (high-diversity) ancestry to each window (summary statistics for each window are given in  
438 **Supplementary Table 2**). This was performed both for the subset of 57 samples (**Figure 1c**) and for  
439 all 161 samples (**Supplementary Figure 6**). Using different window sizes (150, 100 and 50 SNPs  
440 with overlap of 75, 50 and 25 respectively) yielded qualitatively the same results. Intermediate values  
441 in PC1 (between 0.25 and 0.75) were only observed in few, sequential windows where samples

442 transitioned between clusters (**Supplementary Figure 3**). The only exception was sample JB1207,  
443 which we found to be diploid (for details see below).

444

#### 445 **Population structure after hybridization**

446 To characterise the genome-wide distribution of ancestry components along the genome, we ran a  
447 hierarchical cluster analysis on the matrix containing ancestry information (*Sp* or *Sk*) for each window  
448 (columns) and strain (rows) using the R package *Pvclust 2.0.0* (Suzuki and Shimodaira, 2006). *Pvclust*  
449 includes a multiscale bootstrap resampling approach to calculate approximately unbiased probability  
450 values (p-values) for each cluster. We specified 1000 bootstraps using the Ward method and a  
451 Euclidian-based dissimilarity matrix. The analysis was run both for the whole genome (**Figure 1c**) and  
452 by chromosome (**Figure 1c, Supplementary Figure 9**).

453

#### 454 **Phylogenetic analysis of the mitochondrial genome**

455 From the VCF file, we extracted mitochondrial variants for all 161 samples (Jeffares et al., 2015) and  
456 generated an alignment in *.fasta* format by substituting SNPs into the reference *S. pombe* 972 h-  
457 reference genome (ASM294v264) using the package *vcf2fasta*  
458 (<https://github.com/JoseBlanca/vcf2fasta/>, version Nov. 2015). We excluded variants in mitochondrial  
459 regions with SVs inferred from long reads. A maximum likelihood tree was calculated using *RaxML*  
460 (version 8.2.10-gcc-mpi) (Stamatakis, 2014) with default parameters, GTRGAMMAI approximation,  
461 final optimization with GTR + GAMMA + I and 1000 bootstraps. The final tree was visualised using  
462 *FigTree* 1.4.3 (<http://tree.bio.ed.ac.uk/software/figtree/>) (**Supplementary Figure 10**).

463

#### 464 **Time of hybridization**

465 Previous work (Jeffares et al., 2015) has shown that the time to the most recent common ancestor for  
466 161 samples dates back to around 2300 years ago. This defines the maximum boundary for the time of  
467 hybridization. We used the theoretical model by Janzen et al., (2018) to infer the age of the initial  
468 hybridization event. The model predicts the number of ancestry blocks and junctions present in a  
469 hybrid individual as a function of time and effective population size ( $N_e$ ). First, we obtained an  
470 estimate of  $N_e$  using the multiple sequential Markovian coalescent (MSMC). We constructed artificial  
471 diploid genomes from strains with consistent clustering by ancestry (**Figure 1c**) and estimated change  
472 in  $N_e$  as function across time using *MSMC 2-2.0.0* (Schiffels and Durbin, 2014). In total we took four  
473 samples per group and produced diploid genomes in all possible six pairs for each group, except for  
474 one cluster that had only two samples (JB1205 and JB1206). Bootstraps were produced for each  
475 analysis, subsampling 25 genomic fragments per chromosome of 200 kb each. Resulting effective  
476 population size and time was scaled using reported mutation rate of  $2 \cdot 10^{-10}$  mutations site<sup>-1</sup> generation<sup>-1</sup>  
477 (Farlow et al., 2015). Although it is difficult to be certain of the number of independent hybridization  
478 events, it is interesting to see that some clusters show similar demographic histories (**Supplementary**

479 **Figure 24).** Regardless of the demographic history in each cluster, long-term  $N_e$  as estimated by the  
480 harmonic mean ranged between  $1 \cdot 10^5$  and  $1 \cdot 10^9$ .  $N_e$  of the near-pure ancestral *Sp* and *Sk* cluster was  
481  $7 \cdot 10^5$  and  $9 \cdot 10^6$ , respectively. These estimates of  $N_e$  are consistent with previous reports of  $1 \cdot 10^7$   
482 (Farlow et al., 2015).

483

484 We then used a customised R script with the ancestral component matrix to estimate the number of  
485 ancestry blocks (*Sp* or *Sk* clade) (**Supplementary Figure 12**). We used the R script from Janzen et al.,  
486 (2018), and ran the model in each sample and chromosome using:  $N_e = 1 \cdot 10^6$ ,  $r$  = number of genomic  
487 windows per chromosome,  $h0 = 0.298$  (mean heterogeneity ( $h0$ ) was estimated from the ancestral  
488 haplotype matrix) and  $c = 7.1, 5.6,$  and  $4.1$  respectively for chromosome I, II and III (values taken  
489 from Munz et al. (1989)) (**Supplementary Figure 13**). Given the large  $N_e$ , no changes in mean  
490 heterogeneity is expected over time after hybridization due to drift (the proportion of ancestral  
491 haplotypes *Sp* and *Sk* in hybrids, estimated as  $2pq$ , where  $p$  and  $q$  are the proportion of each ancestral  
492 clade in hybrids). Accordingly, results did not change within the range of the large  $N_e$  values. For this  
493 analysis, samples with proportion of admixture lower than 0.1 were excluded. The analysis was  
494 repeated with different windows sizes (200, 100 and 50 SNPs per window).

495

#### 496 **Demographic validation**

497 To differentiate between possible historical scenarios underlying the observed pattern of ancestral  
498 divergence and introgression we performed individual based forward simulations using *SLiM 3.2.1*  
499 (Haller and Messer, 2019). These simulations were not intended to trace the “real” demographic  
500 history including estimates of split time, changes in effective population size, population structure  
501 after hybridization, or migration rates between subpopulations. Much rather, we contrasted two  
502 extremes of a continuum of possible scenarios: i) a scenario of ancestral divergence in isolation  
503 followed by a short, recent period of gene flow and ii) a scenario of divergence with continuous gene  
504 flow throughout the course of evolution. We asked the questions which of the simulated scenarios may  
505 better recover the empirically observed deep divergence of ancestry components and their distribution  
506 in blocks along the genome. We parametrized the simulations with estimates from the literature  
507 including  $1 \cdot 10^6$  for  $N_e$ , a mutation rate of  $2 \cdot 10^{-10}$  site<sup>-1</sup> generation<sup>-1</sup> (Farlow et al., 2015), an average  
508 recombination rate of  $1 \cdot 10^6$  site<sup>-1</sup> generation<sup>-1</sup> (Munz et al., 1989), and a cloning rate of 0.95  
509 generation<sup>-1</sup> (equivalent to around 1 sexual cycle every 20 asexual generations). In order to reduce the  
510 computational effort, all parameters were scaled relative to a  $N_e$  of 1000 as suggested in the SLiM  
511 manual. Simulations were divided in two parts: 1) simulations of single 15 kb genomic windows  
512 corresponding to  $\sim 200$  SNPs per window in the empirical data; 2) whole chromosome simulations  
513 with a fragment of 3 Mb corresponding to the size of *S. pombe* chromosome III. In both cases, we  
514 simulated divergence of two populations that were connected by different levels of symmetrical gene  
515 flow ranging from migration rates of 0 (complete isolation) to  $1 \cdot 10^{-4}$  (equivalent to 100 migrants per

516 generation in a population of  $1 \cdot 10^6$ ). To mimic the empirical difference in genetic diversity between  
517 populations, effective population sizes of the populations were set to  $7 \cdot 10^5$  and  $3 \cdot 10^5$ , respectively. For  
518 the first part (single windows), a total of 100 replicate simulations were run for  $30 \cdot N_e$  generations.  
519 Every  $2 N_e$  generations 50 individuals were randomly sampled in total from both populations. At each  
520 time point, samples were processed in the same way as the empirical data per window estimating the  
521 percentage of variance explained by PC1 and  $D_{xy}$  between subgroups as inferred by normalized PC1  
522 scores (**Supplementary Figure 7**). For the second part (whole chromosome), a total of 100 replicate  
523 simulations were run for  $15 \cdot N_e$  generations after which a total of 50 genomes were randomly sampled  
524 from both populations. Simulated data were divided into genomic windows of 200 SNPs and  
525 processed in the same way as the empirical data (**Supplementary Figure 8**) for which the mean  
526 proportion of variance explained by PC1 was 64% and mean divergence between subpopulations ( $D_{xy}$ )  
527 was 0.0058. These values were only obtained in the simulations of a single genomic window under  
528 migration rates below  $2 \cdot 10^{-5}$  (equivalent to 20 migrants per generation in a population of  $1 \cdot 10^6$   
529 individuals). However, this migration rate was not enough to produce recombinant blocks in whole  
530 chromosome simulations. Blocks were only observed when migration rate exceeded  $1 \cdot 10^{-4}$  (100  
531 migrants per generation). Yet, with this level of gene flow the proportion of variance explained by  
532 PC1 (around 25% in all simulations) and  $D_{xy}$  (below 0.0025 in all simulations) were significantly  
533 lower.

534

### 535 **Phenotypic variation and reproductive isolation**

536 We sourced phenotypic data of 229 phenotypic measurements in the 161 strains including amino acid  
537 quantification on liquid chromatography (aaconc), growth and stress on solid media (smgrowth), cell  
538 growth parameters and kinetics in liquid media (lmgrowth) and cell morphology (shape1 and shape2)  
539 from Jeffares et al. (2015). Data on reproductive isolation measured as the percentage of viable spores  
540 in pairs of crosses were compiled from Jeffares et al. (2015) and Marsellach (2017). A summary of all  
541 phenotypic measurements and reproductive data is provided in **Supplementary Table 4 and 5**,  
542 respectively.

543

544 First, we normalized each phenotypic trait  $y$  using rank-based transformation with the relationship  
545  $\text{normal.y} = \text{qnorm}(\text{rank}(y) / (1 + \text{length}(y)))$ . We then conducted PCA on normalized values of  
546 all phenotypic traits using the R package *missMDA* 1.12 (Josse and Husson, 2016). We estimated the  
547 number of dimensions for the principal component analysis by cross-validation, testing up to 30 PC  
548 components and imputing missing values. In addition to PCA decomposing variance across all traits,  
549 we examined the effect of admixture on each trait separately. Samples were divided into three discrete  
550 categories of admixture: two groups including samples with low admixture proportions (proportion of  
551 *Sp* or *Sk* clades higher than 0.9), and one for hybrid samples (proportion of *Sp* or *Sk* clades between  
552 0.1 to 0.9). Significant differences in phenotypic distributions between groups were tested using *Tukey*



553 *Honest Significant Differences* as implemented in *Stats 3.4.2* (Team, 2014). **Supplementary Figure**  
554 **14** shows the distribution of phenotypic values by admixture category for each trait. The number of  
555 traits with significant differences among groups was contrasted to values obtained by randomising  
556 admixture categories without replacement (permutations of the *Sp*, *Sk*, or *hybrid* category). Observed  
557 values were contrasted with distribution of the expected number of significant traits after running  
558 10000 independent permutations (**Supplementary Figure 15**).

559

#### 560 **Heritability**

561 Heritability was estimated for all normalized traits using *LDAK 5.94* (Speed et al., 2012), calculating  
562 independent kinship matrices derived from: 1) all SNPs and 2) ancestral haplotypes. Both SNPs and  
563 haplotype data were binary encoded (0 or 1). Jeffares et al. (2015) showed that heritability estimates  
564 between normalised and raw values are highly correlated ( $r = 0.69$ ,  $p\text{-value} \leq 2.2 \cdot 10^{-16}$ ). Heritability  
565 estimated with SNP values were strongly correlated with those from ancestral haplotypes ( $r = 0.82$ ,  $p\text{-}$   
566  $\text{value} \leq 2.2 \cdot 10^{-16}$ ). Heritability estimates and standard deviation for each trait for both SNPs and  
567 ancestral haplotypes are detailed in **Supplementary Table 6**.

568

#### 569 **Identification of ploidy changes**

570 *S. pombe* is generally considered haploid under natural conditions. Yet, for two samples ancestry  
571 components did not separate on the principle component axis 1 (see above) for much of the genome.  
572 Instead, these samples were intermediate in PC1 score. A possible explanation is diploidisation of the  
573 two ancestral genomes. To establish the potential ploidy of samples, we called variants for all 161  
574 samples using the Illumina data from Jeffares *et al* (2015) . Cleaned reads were mapped with *BWA*  
575 (version 0.7.17-r1188) in default settings and variants were called using *samtools* and *bcftools* (version  
576 1.8). After filtering reads with a QUAL score  $> 25$ , the number of heterozygous sites per base per  
577 20kb window were calculated. Additionally the nuclear content (C) as measured by Jeffares et al.  
578 (2015) (Supplementary Table S4 in Jeffares *et al* (2015)) were used to verify increased ploidy. Two  
579 samples showed high heterozygosity along the genome (JB1169 and JB1207) of which JB1207 for  
580 which data were available also showed a high C-value, suggesting that these samples are diploid  
581 (**Supplementary Figures 4 & 25**). In JB1207, heterozygosity varies along the genome, with regions  
582 of high and low diversity. Sample JB1110 showed genomic content similar to JB1207, but did not  
583 show heterozygosity levels above that of haploid strains, suggesting the increase in genome content  
584 occurred by autopoloidization.

585

#### 586 **High-weight genomic DNA extraction and whole genome sequencing**

587 To obtain high weight gDNA for long-read sequencing, we grew strains from single colonies and  
588 cultured them in 200 mL liquid EMM at 32 °C shaking at 150 r.p.m. overnight. Standard media and  
589 growth conditions were used throughout this work (Hagan et al., 2016) with minor modifications: We

590 used standard liquid Edinburgh Minimal Medium (EMM; Per liter: Potassium Hydrogen Phthalate  
591 3.0 g, Na HPO<sub>4</sub>·2H<sub>2</sub>O 2.76 g, NH<sub>4</sub>Cl 5.0 g, D-glucose 20 g, MgCl<sub>2</sub>·6H<sub>2</sub>O 1.05 g, CaCl<sub>2</sub>·2H<sub>2</sub>O  
592 14.7 mg, KCl 1 g, Na<sub>2</sub>SO<sub>4</sub> 40 mg, Vitamin Stock ×1000 1.0 ml, Mineral Stock ×10,000 0.1 ml,  
593 supplemented with 100 mg l<sup>-1</sup> adenine and 225 mg l<sup>-1</sup> leucine) for the asexual growth. DNA extraction  
594 was performed with Genomic Tip 500/G or 100/G kits (Qiagen) following the manufacturer's  
595 instruction, but using Lallzyme MMX for lysis (Flor-Parra et al 2014, doi:10.1002/yea.2994). For each  
596 sample, 20 kb libraries were produced that were sequenced on one SMRT cell per library using the  
597 Pacific Biosciences RSII Technology Platform (PacBio®, CA). For a subset of eight samples,  
598 additional sequencing was performed using Oxford Nanopore (MinION). Sequencing was performed  
599 at SciLifeLab, Uppsala, Gene centre LMU, Munich and the Genomics & Bioinformatics Laboratory,  
600 University of York. We obtained on average 80x (SMRT) and 140x (nanopore) coverage for the  
601 nuclear genome for each sample (summary in **Supplementary Table 7**).

602

603 Additionally, 2.5 µg of the same DNA was delivered to the SNP&SEQ Technology Platform at the  
604 Uppsala Biomedical Centre (BMC), for Illumina sequencing. Libraries were prepared using the  
605 TruSeq PCRfree DNA library preparation kit (Illumina Inc.). Sequencing was performed on all  
606 samples pooled into a single lane, with cluster generation and 150 cycles paired-end sequencing on the  
607 HiSeqX system with v2.5 sequencing chemistry (Illumina Inc.). These data were used for draft  
608 genome polishing (see below).

609

#### 610 ***De novo* assembly of single-molecule read data**

611 *De novo* genomes were assembled with *Canu* 1.5 (Koren et al., 2017) using default parameters.  
612 BridgeMapper from the *SMRT* 2.3.0 package was used to polish and subsequently assess the quality of  
613 genome assembly. Draft genomes were additionally polishing using short Illumina reads, running four  
614 rounds of read mapping to the draft genome with *BWA* 0.7.15 and polishing with *Pilon* 1.22 (Walker  
615 et al., 2014). Summary statistics of the final assembled genomes are found in **Supplementary Table 7**.

616 *De novo* genomes were aligned to the reference genome using *MUMmer* 3.23 (Kurtz et al., 2004).  
617 Contigs were classified by reference chromosome to which they showed the highest degree of  
618 complementary. We used customised python scripts to identify and trim mitochondrial genomes.

619

#### 620 **Structural variant detection**

621 Structural variants (SVs) were identified by a combination of a *de novo* and mapping approach. *De*  
622 *nov*o genomes were aligned to the reference genome using *MUMmer*, and SVs were called using the  
623 function show-diff and the package *SVMU* 0.2beta (Khost et al., 2017). Then, raw long reads were  
624 mapped to the reference genome with *NGMLR* and genotypes were called using the package *Sniffles*  
625 (Sedlazeck et al., 2018). We implemented a new function within Sniffles “forced genotypes”, which  
626 calls SVs by validating the mapping calls from an existing list of breaking points or SVs. This reports

627 the read support per variant even down to a single read. We forced genotypes using the list of *de novo*  
628 breaking points to generate a multi-sample VCF file. SVs were merged using the package *SURVIVOR*  
629 (Jeffares et al., 2017) option merge with a threshold of 1kbp and requiring the same type. In total, it  
630 resulted in a list of 1498 SVs with 892 in common between the mapping and *de-novo* approaches  
631 **(Supplementary Figure 16)**.

632

633 Within the 892 common variants we compared the accuracy of genotyping between sample by  
634 comparing genotypes obtained from *de novo* genomes and by mapping reads to reference genome.  
635 Additionally, we compared genotypes in samples sequenced with both PacBio and MinIon. In total we  
636 sequenced 8 samples with both technologies. We found high consistency for variants called with both  
637 sequencing technologies and observed that allele frequencies were highly correlated ( $r = 0.98$ , p-value  
638  $\leq 2.2 \times 10^{-16}$ ) **(Supplementary Figures 16 - 19)**.

639 Only common SVs between the mapping and *de-novo* approach were considered, and variants with  
640 consistency below 50% were removed. We manually checked large SVs (larger than 10kb) by  
641 comparing the list of SVs with the alignment of the *de novo* genomes to the reference genome from  
642 MUMmer. This resulted in a final data set with 832 SVs **(Supplementary Table 8)**.

643

#### 644 **Distribution of SVs around developmentally programmed DNA double-strand breaks (DSB)**

645 We tested the association between DSB and SVs by comparing the physical genomic coordinates of  
646 the final list of SVs with DSB locations accessed from Fowler et al., (2014). Maintaining the same  
647 number of SVs per chromosome, we used a customized R script to randomise SV coordinates and  
648 measure the distances to the closest DSB. We counted the number of SVs present within different  
649 intervals of physical genetic distance ([0,500), [500, 1000), [1000, 2000), [2000, 4000), [4000, 10000),  
650 [10000, 20000), [20000, 30000) bp). Empirically observed values were contrasted with randomized  
651 distribution after running 10000 independent permutations. P-values of differences between  
652 randomization and observed values were obtained from the fraction of expected values higher than the  
653 observed value from the original data **(Supplementary Figures 20)**.

654

#### 655 **PCR validation of large SVs**

656 To test the frequency of large inversions and rearrangements observed from long read data, we  
657 performed PCR verification over the breakpoints in the 57 non-clone samples. PCR was performed for  
658 both sides of the breakpoints, with a combination of one primer ‘outside’ of the inversion and both  
659 primers ‘inside’ the inversion **(Supplementary Figure 26)**. PCR were performed on DNA using  
660 standard *Taq* polymerase, with annealing temperature at 59°C. The primers used, the coordinates in  
661 the reference and the expected amplicon length are given in **Supplementary Table 9**.

662

663 **Distribution of structural variants in ancestral population – Two dimensional folded site**  
664 **frequency spectrum**

665 We used the location of break points of SVs to identify whether a variant was located in the *Sp* or *Sk*  
666 genetic background in each sample. Ancestral haplotypes are difficult to infer in telomeric and  
667 centromeric regions given the low confidence in SNP calling in those regions, resulting in low  
668 percentage of variance explained by PC1. Thus SVs with break points in those regions were excluded  
669 from this analysis (19 SVs). SVs were grouped by ancestral group and allele frequencies were  
670 calculated for each ancestral population. We used these frequencies to build a two dimensional folded  
671 site frequency spectrum (2dSFS). In order to compare this 2dSFS, we repeated the analysis using SNP  
672 data from all 57 samples. Considering that the majority of identified SVs with long reads were  
673 transposable elements, we also made use of LRT insertion-deletion polymorphism (indels) inferred  
674 from short reads. For this additional data we produced a similar folded 2d SFS. LTR indel data were  
675 taken from Jeffares et al., (2015) and are listed in **Supplementary Table 11**.

676

677 **Decay in linkage disequilibrium (LD)**

678 To contrast LD between alleles from alternative ancestral groups, we calculated LD between all  
679 described genomic windows within chromosomes (**Supplementary Figure 22**). For this analysis only  
680 hybrid samples were considered (strains with admixture proportion higher than 0.1). For each pair of  
681 windows, we polarized windows by ancestry (at a threshold of > 0.7) and calculated standardized LD  
682 as the squared Pearson's correlation coefficient ( $R^2$ ) (Hill and Robertson, 1968; Weir, 1979). This  
683 measurement takes into consideration difference in allele frequencies. The expected value of  $R^2$   
684 ( $E(R^2)$ ) can be approximated by (Hill and Weir, 1988):

685 
$$E(R^2) = \left( \frac{10 + C}{(2 + C) * (11 + C)} \right) * \left( 1 + \frac{(3 + C) * (12 + 12C + C^2)}{n * (2 + C) * (11 + C)} \right)$$

686 Where C corresponds to product between the genetic distance (bp) and the population recombination  
687 rate ( $\rho$ ) in n number of haplotype sampled. The population recombination rate was calculated as:  $\rho =$   
688  $4 * N_e * c$ , where c is the recombination fraction between sites and  $N_e$  is the effective population size.  
689 We fitted a nonlinear model to obtain least squares estimates of  $\rho$  using a customized R script. The  
690 decay of LD with physical distance can be described with this model (Remington et al., 2001). LD  
691 values were grouped in three categories: i) comparison between windows with high proportion  
692 ( $Sp > 0.7$ ) of *Sp* ancestral group (*Sp-Sp*); ii) high proportion ( $Sk > 0.7$ ) of *Sk* ancestral group (*Sk-Sk*); and  
693 iii) high proportion of opposite ancestral groups (*Sp-Sk*). i) and ii) represent cases of positive ancestry  
694 disequilibrium, iii) will be denoted as negative ancestry disequilibrium. In order to reduce bias given  
695 the potential for secondary population structure (clusters in **Figure 1c**), the analysis was repeated  
696 using one random sample per cluster, resulting in similar general conclusions (**Supplementary Figure**  
697 **27**).

698

699 **Data availability**

700 Nanopore, single-molecule real time sequencing data and de-novo genomes are available at NCBI  
701 Sequence Read Archive, BioProject ID PRJNA527756.

702

703 **Acknowledgments**

704

705 We thank Fidel Botero-Castro, Ana Catalán, Sebastian Höhna, Ulrich Knief, Claire Peart, Joshua  
706 Peñalba, Ricardo Pereira, Matthias Weissensteiner, (LMU Munich) and S. Lorena Ament-Velásquez  
707 (Uppsala University) for providing valuable intellectual input on the various analyses, sharing scripts  
708 and critically comment on the manuscript. We are further indebted to Bernadette Weissensteiner for  
709 extensive help with laboratory work and Saurabh Pophaly for bioinformatics support (LMU Munich).  
710 We further acknowledge support for data generation from the National Genomics Infrastructure,  
711 Uppsala, Sweden, the Gene Centre, Munich, Germany, Sally James and Peter Ashton from the  
712 Bioscience Technology Facility, Department of Biology, University of York, U.K, and James Chong,  
713 Department of Biology, University of York, U.K. The computational infrastructure was provided by  
714 the UPPMAX Next-Generation Sequencing Cluster and Storage (UPPNEX) project funded by the  
715 Knut and Alice Wallenberg Foundation and the Swedish National Infrastructure for Computing and  
716 the York Advanced Research Computing Cluster (YARCC), University of York, U.K. This study was  
717 funded by LMU Munich to JW and NHGRI UM1 HG008898 to FS.

718

719 **References**

720

- 721 Abbott, R., Albach, D., Ansell, S., Arntzen, J.W., Baird, S.J.E., Bierne, N., Boughman, J.,  
722 Brelsford, A., Buerkle, C.A., Buggs, R., Butlin, R.K., Dieckmann, U., Eroukhanoff,  
723 F., Grill, A., Cahan, S.H., Hermansen, J.S., Hewitt, G., Hudson, A.G., Jiggins, C.,  
724 Jones, J., Keller, B., Marczewski, T., Mallet, J., Martinez-Rodriguez, P., Möst, M.,  
725 Mullen, S., Nichols, R., Nolte, A.W., Parisod, C., Pfennig, K., Rice, A.M., Ritchie,  
726 M.G., Seifert, B., Smadja, C.M., Stelkens, R., Szymura, J.M., Väinölä, R., Wolf,  
727 J.B.W., Zinner, D., 2013. Hybridization and speciation. *J. Evol. Biol.* 26, 229–246.  
728 <https://doi.org/10.1111/j.1420-9101.2012.02599.x>
- 729 Abbott, R.J., Barton, N.H., Good, J.M., 2016. Genomics of hybridization and its evolutionary  
730 consequences. *Mol. Ecol.* 25, 2325–2332. <https://doi.org/10.1111/mec.13685>
- 731 Brown, W.R.A., Liti, G., Rosa, C., James, S., Roberts, I., Robert, V., Jolly, N., Tang, W.,  
732 Baumann, P., Green, C., Schlegel, K., Young, J., Hirschfeld, F., Leek, S., Thomas, G.,  
733 Blomberg, A., Warringer, J., 2011. A Geographically Diverse Collection of  
734 *Schizosaccharomyces pombe* Isolates Shows Limited Phenotypic Variation but  
735 Extensive Karyotypic Diversity. *G3 GenesGenomesGenetics* 1, 615–626.  
736 <https://doi.org/10.1534/g3.111.001123>
- 737 Corbett-Detig, R.B., Zhou, J., Clark, A.G., Hartl, D.L., Ayroles, J.F., 2013. Genetic  
738 incompatibilities are widespread within species. *Nature* 504, 135–137.  
739 <https://doi.org/10.1038/nature12678>

740 Currall, B.B., Chiangmai, C., Talkowski, M.E., Morton, C.C., 2013. Mechanisms for  
741 Structural Variation in the Human Genome. *Curr. Genet. Med. Rep.* 1, 81–90.  
742 <https://doi.org/10.1007/s40142-013-0012-8>

743 Dowling, T. E., Smith, G. R. & Brown, W. M. Reproductive isolation and introgression  
744 between *Notropis cornutus* and *Notropis chrysocephalus* (family Cyprinidae):  
745 comparison of morphology, allozymes, and mitochondrial DNA. *Evolution*. **43**, 620–  
746 634 (1989).

747 Eroukhmanoff, F., Hermansen, J.S., Bailey, R.I., Sæther, S.A., Sætre, G.-P., 2013. Local  
748 adaptation within a hybrid species. *Heredity* 111, 286–292.  
749 <https://doi.org/10.1038/hdy.2013.47>

750 Faria, R., Navarro, A., 2010. Chromosomal speciation revisited: rearranging theory with  
751 pieces of evidence. *Trends Ecol. Evol.* 25, 660–669.  
752 <https://doi.org/10.1016/j.tree.2010.07.008>

753 Farlow, A., Long, H., Arnoux, S., Sung, W., Doak, T.G., Nordborg, M., Lynch, M., 2015. The  
754 Spontaneous Mutation Rate in the Fission Yeast *Schizosaccharomyces pombe*.  
755 *Genetics* 201, 737–744. <https://doi.org/10.1534/genetics.115.177329>

756 Fawcett, J.A., Iida, T., Takuno, S., Sugino, R.P., Kado, T., Kugou, K., Mura, S., Kobayashi,  
757 T., Ohta, K., Nakayama, J., Innan, H., 2014. Population Genomics of the Fission  
758 Yeast *Schizosaccharomyces pombe*. *PLOS ONE* 9, e104241.  
759 <https://doi.org/10.1371/journal.pone.0104241>

760 Fisher, R.A., 1999. *The genetical theory of natural selection: a complete variorum edition*.  
761 Oxford University Press.

762 Fowler, K.R., Sasaki, M., Milman, N., Keeney, S., Smith, G.R., 2014. Evolutionarily diverse  
763 determinants of meiotic DNA break and recombination landscapes across the genome.  
764 *Genome Res.* 24, 1650–1664. <https://doi.org/10.1101/gr.172122.114>

765 Hagan, I.M., Carr, A.M., Grallert, A., Nurse, P., 2016. *Fission yeast: a laboratory manual*.  
766 Cold Spring Harbor Laboratory Press.

767 Haller, B.C., Messer, P.W., 2019. SLiM 3: Forward Genetic Simulations Beyond the Wright–  
768 Fisher Model. *Mol. Biol. Evol.* 36, 632–637. <https://doi.org/10.1093/molbev/msy228>

769 Hill, W.G., Robertson, A., 1968. Linkage disequilibrium in finite populations. *Theor. Appl.*  
770 *Genet.* 38, 226–231. <https://doi.org/10.1007/BF01245622>

771 Hill, W.G., Weir, B.S., 1988. Variances and covariances of squared linkage disequilibria in  
772 finite populations. *Theor. Popul. Biol.* 33, 54–78. [https://doi.org/10.1016/0040-5809\(88\)90004-4](https://doi.org/10.1016/0040-5809(88)90004-4)

773

774 Hoffman, C.S., Wood, V., Fantes, P.A., 2015. An Ancient Yeast for Young Geneticists: A  
775 Primer on the *Schizosaccharomyces pombe* Model System. *Genetics* 201, 403–423.  
776 <https://doi.org/10.1534/genetics.115.181503>

777 Hoffmann, A.A., Rieseberg, L.H., 2008. Revisiting the Impact of Inversions in Evolution:  
778 From Population Genetic Markers to Drivers of Adaptive Shifts and Speciation? *Annu.*  
779 *Rev. Ecol. Evol. Syst.* 39, 21–42.  
780 <https://doi.org/10.1146/annurev.ecolsys.39.110707.173532>

781 Hu, W., Jiang, Z.-D., Suo, F., Zheng, J.-X., He, W.-Z., Du, L.-L., 2017. A large gene family  
782 in fission yeast encodes spore killers that subvert Mendel’s law. *eLife* 6.  
783 <https://doi.org/10.7554/eLife.26057>

784 Janzen, T., Nolte, A. W. & Traulsen, A. The breakdown of genomic ancestry blocks in hybrid  
785 lineages given a finite number of recombination sites: breakdown of ancestry blocks  
786 after hybridization. *Evolution*. **72**, 735–750 (2018).

787 Jay, P., Whibley, A., Frézal, L., Rodríguez de Cara, M.Á., Nowell, R.W., Mallet, J.,  
788 Dasmahapatra, K.K., Joron, M., 2018. Supergene Evolution Triggered by the

789 Introgression of a Chromosomal Inversion. *Curr. Biol.* 28, 1839-1845.e3.  
790 <https://doi.org/10.1016/j.cub.2018.04.072>

791 Jeffares, D.C., 2018. The natural diversity and ecology of fission yeast. *Yeast* 35, 253–260.  
792 <https://doi.org/10.1002/yea.3293>

793 Jeffares, D.C., Jolly, C., Hoti, M., Speed, D., Shaw, L., Rallis, C., Balloux, F., Dessimoz, C.,  
794 Bähler, J., Sedlazeck, F.J., 2017. Transient structural variations have strong effects on  
795 quantitative traits and reproductive isolation in fission yeast. *Nat. Commun.* 8, 14061.  
796 <https://doi.org/10.1038/ncomms14061>

797 Jeffares, D.C., Rallis, C., Rieux, A., Speed, D., Přeborovský, M., Mourier, T., Marsellach,  
798 F.X., Iqbal, Z., Lau, W., Cheng, T.M.K., Pracana, R., Mülleder, M., Lawson, J.L.D.,  
799 Chessel, A., Bala, S., Hellenthal, G., O’Fallon, B., Keane, T., Simpson, J.T., Bischof,  
800 L., Tomiczek, B., Bitton, D.A., Sideri, T., Codlin, S., Hellberg, J.E.E.U., van Trigt, L.,  
801 Jeffery, L., Li, J.-J., Atkinson, S., Thodberg, M., Febrer, M., McLay, K., Drou, N.,  
802 Brown, W., Hayles, J., Salas, R.E.C., Ralser, M., Maniatis, N., Balding, D.J., Balloux,  
803 F., Durbin, R., Bähler, J., 2015. The genomic and phenotypic diversity of  
804 *Schizosaccharomyces pombe*. *Nat. Genet.* 47, 235–241.  
805 <https://doi.org/10.1038/ng.3215>

806 Josse, J., Husson, F., 2016. missMDA: A Package for Handling Missing Values in  
807 Multivariate Data Analysis. *J. Stat. Softw.* 70. <https://doi.org/10.18637/jss.v070.i01>

808 Kelly, F.D., Levin, H.L., 2005. The evolution of transposons in *Schizosaccharomyces pombe*.  
809 *Cytogenet. Genome Res.* 110, 566–574. <https://doi.org/10.1159/000084990>

810 Khost, D.E., Eickbush, D.G., Larracuente, A.M., 2017. Single-molecule sequencing resolves  
811 the detailed structure of complex satellite DNA loci in *Drosophila melanogaster*.  
812 *Genome Res.* 27, 709–721. <https://doi.org/10.1101/gr.213512.116>

813 Kondrat’eva, V.I., Naumov, G.I., 2001. The Phenomenon of Spore Killing in  
814 *Schizosaccharomyces pombe* Hybrids. *Dokl. Biol. Sci.* 379, 385–388.  
815 <https://doi.org/10.1023/A:1011624918673>

816 Koren, S., Walenz, B.P., Berlin, K., Miller, J.R., Bergman, N.H., Phillippy, A.M., 2017.  
817 Canu: scalable and accurate long-read assembly via adaptive *k*-mer weighting and  
818 repeat separation. *Genome Res.* 27, 722–736. <https://doi.org/10.1101/gr.215087.116>

819 Küpper, C., Stocks, M., Risse, J.E., dos Remedios, N., Farrell, L.L., McRae, S.B., Morgan,  
820 T.C., Karlionova, N., Pinchuk, P., Verkuil, Y.I., Kitaysky, A.S., Wingfield, J.C.,  
821 Piersma, T., Zeng, K., Slate, J., Blaxter, M., Lank, D.B., Burke, T., 2016. A supergene  
822 determines highly divergent male reproductive morphs in the ruff. *Nat. Genet.* 48, 79–  
823 83.

824 Kurtz, S., Phillippy, A., Delcher, A.L., Smoot, M., Shumway, M., Antonescu, C., Salzberg,  
825 S.L., 2004. Versatile and open software for comparing large genomes. *Genome Biol.* 5,  
826 R12.

827 Lamichhaney, S. *et al.* Rapid hybrid speciation in Darwin’s finches. *Science* eaao4593 (2017).

828 Leducq, J.-B., Nielly-Thibault, L., Charron, G., Eberlein, C., Verta, J.-P., Samani, P.,  
829 Sylvester, K., Hittinger, C.T., Bell, G., Landry, C.R., 2016. Speciation driven by  
830 hybridization and chromosomal plasticity in a wild yeast. *Nat. Microbiol.* 1, 15003.  
831 <https://doi.org/10.1038/nmicrobiol.2015.3>

832 Mallet, J., 2007. Hybrid speciation. *Nature* 446, 279–283.  
833 <https://doi.org/10.1038/nature05706>

834 Mallet, J., 2005. Hybridization as an invasion of the genome. *Trends Ecol. Evol.* 20, 229–237.

835 Marsellach, X. A non-genetic meiotic repair program inferred from spore survival values in  
836 fission yeast wild isolates: a clue for an epigenetic ratchet-like model of ageing?  
837 (2017).

838 McDonald, M.J., Rice, D.P., Desai, M.M., 2016. Sex speeds adaptation by altering the  
839 dynamics of molecular evolution. *Nature* 531, 233–236.  
840 <https://doi.org/10.1038/nature17143>

841 Meier, J.I., Marques, D.A., Mwaiko, S., Wagner, C.E., Excoffier, L., Seehausen, O., 2017.  
842 Ancient hybridization fuels rapid cichlid fish adaptive radiations. *Nat. Commun.* 8,  
843 ncomms14363. <https://doi.org/10.1038/ncomms14363>

844 Muller, H.J., 1932. Some genetic aspects of sex. *Am. Nat.* 66, 118–138.

845 Munz, P., Wolf, K., Kohli, J., Leupold, U., 1989. Genetics overview. *Mol. Biol. Fission Yeast*  
846 1–30.

847 Naumov, G.I., Kondratieva, V.I., Naumova, E.S., 2015. Hybrid sterility of the yeast  
848 *Schizosaccharomyces pombe*: Genetic genus and many species in statu nascendi?  
849 *Microbiology* 84, 159–169. <https://doi.org/10.1134/S0026261715010099>

850 Nei, M., Li, W.H., 1979. Mathematical model for studying genetic variation in terms of  
851 restriction endonucleases. *Proc. Natl. Acad. Sci.* 76, 5269–5273.  
852 <https://doi.org/10.1073/pnas.76.10.5269>

853 Nieto Feliner, G., Álvarez, I., Fuertes-Aguilar, J., Heuertz, M., Marques, I., Moharrek, F.,  
854 Piñeiro, R., Riina, R., Rosselló, J.A., Soltis, P.S., Villa-Machío, I., 2017. Is homoploid  
855 hybrid speciation that rare? An empiricist’s view. *Heredity* 118, 513–516.  
856 <https://doi.org/10.1038/hdy.2017.7>

857 Nieuwenhuis, B.P.S., Tusso, S., Bjerling, P., Stångberg, J., Wolf, J.B.W., Immler, S., 2018.  
858 Repeated evolution of self-compatibility for reproductive assurance. *Nat. Commun.* 9.  
859 <https://doi.org/10.1038/s41467-018-04054-6>

860 Nolte, A.W., Sheets, H.D., 2005. Shape based assignment tests suggest transgressive  
861 phenotypes in natural sculpin hybrids (Teleostei, Scorpaeniformes, Cottidae). *Front.*  
862 *Zool.* 2, 11. <https://doi.org/10.1186/1742-9994-2-11>

863 Nuckolls, N.L., Bravo Núñez, M.A., Eickbush, M.T., Young, J.M., Lange, J.J., Yu, J.S.,  
864 Smith, G.R., Jaspersen, S.L., Malik, H.S., Zanders, S.E., 2017. wtf genes are prolific  
865 dual poison-antidote meiotic drivers. *eLife* 6. <https://doi.org/10.7554/eLife.26033>

866 Ortiz-Barrientos, D., Engelstädter, J., Rieseberg, L.H., 2016. Recombination Rate Evolution  
867 and the Origin of Species. *Trends Ecol. Evol.* 31, 226–236.  
868 <https://doi.org/10.1016/j.tree.2015.12.016>

869 Payseur, B. A. & Rieseberg, L. H. A genomic perspective on hybridization and speciation.  
870 *Mol. Ecol.* n/a-n/a (2016).

871 Pennisi, E., 2016. A shortcut to a species. *Science* 354, 818–818.  
872 <https://doi.org/10.1126/science.354.6314.818>

873 Peter, J., De Chiara, M., Friedrich, A., Yue, J.-X., Pflieger, D., Bergström, A., Sigwalt, A.,  
874 Barre, B., Freel, K., Llored, A., Cruaud, C., Labadie, K., Aury, J.-M., Istace, B.,  
875 Lebrigand, K., Barbry, P., Engelen, S., Lemainque, A., Wincker, P., Liti, G.,  
876 Schacherer, J., 2018. Genome evolution across 1,011 *Saccharomyces cerevisiae*  
877 isolates. *Nature* 556, 339–344. <https://doi.org/10.1038/s41586-018-0030-5>

878 Pfennig, K.S., Kelly, A.L., Pierce, A.A., 2016. Hybridization as a facilitator of species range  
879 expansion. *Proc. R. Soc. B Biol. Sci.* 283, 20161329.  
880 <https://doi.org/10.1098/rspb.2016.1329>

881 Poelstra, J.W., Vijay, N., Bossu, Christen, Lantz, Henrik, Ryll, Bettina, Müller, Inge,  
882 Baglione, Vittorio, Unneberg, Per, Wikelski, Martin, Grabherr, Manfred, Wolf, Jochen  
883 B. W., 2014. The genomic landscape underlying phenotypic integrity in the face of  
884 gene flow in crows. *Science* 344, 1410–1414.

885 Remington, D.L., Thornsberry, J.M., Matsuoka, Y., Wilson, L.M., Whitt, S.R., Doebley, J.,  
886 Kresovich, S., Goodman, M.M., Buckler, E.S., 2001. Structure of linkage



887 disequilibrium and phenotypic associations in the maize genome. *Proc. Natl. Acad. Sci.*  
888 98, 11479–11484. <https://doi.org/10.1073/pnas.201394398>

889 Runemark, A. *et al.* Variation and constraints in hybrid genome formation. *Nat. Ecol. Evol.*  
890 (2018).

891 Sankararaman, S., Mallick, S., Dannemann, M., Prüfer, K., Kelso, J., Pääbo, S., Patterson, N.,  
892 Reich, D., 2014. The genomic landscape of Neanderthal ancestry in present-day  
893 humans. *Nature* 507, 354–357. <https://doi.org/10.1038/nature12961>

894 Schiffels, S., Durbin, R., 2014. Inferring human population size and separation history from  
895 multiple genome sequences. *Nat. Genet.* 46, 919–925. <https://doi.org/10.1038/ng.3015>

896 Schumer, M., Cui, R., Powell, D.L., Rosenthal, G.G., Andolfatto, P., 2016. Ancient  
897 hybridization and genomic stabilization in a swordtail fish. *Mol. Ecol.* 25, 2661–2679.  
898 <https://doi.org/10.1111/mec.13602>

899 Schumer, M., Rosenthal, G. G. & Andolfatto, P. How common is homoploid hybrid  
900 speciation?: Perspective. *Evolution* 68, 1553–1560 (2014).

901 Sedlazeck, F.J., Rescheneder, P., Smolka, M., Fang, H., Nattestad, M., von Haeseler, A.,  
902 Schatz, M.C., 2018. Accurate detection of complex structural variations using single-  
903 molecule sequencing. *Nat. Methods* 15, 461–468. [https://doi.org/10.1038/s41592-018-](https://doi.org/10.1038/s41592-018-0001-7)  
904 0001-7

905 Seehausen, O., 2004. Hybridization and adaptive radiation. *Trends Ecol. Evol.* 19, 198–207.  
906 <https://doi.org/10.1016/j.tree.2004.01.003>

907 Singh, G., Klar, A.J., 2002. The 2.1-kb inverted repeat DNA sequences flank the *mat2*, 3  
908 silent region in two species of *Schizosaccharomyces* and are involved in epigenetic  
909 silencing in *Schizosaccharomyces pombe*. *Genetics* 162, 591–602.

910 Soltis, P.S., Soltis, D.E., 2009. The Role of Hybridization in Plant Speciation. *Annu. Rev.*  
911 *Plant Biol.* 60, 561–588. <https://doi.org/10.1146/annurev.arplant.043008.092039>

912 Speed, D., Hemani, G., Johnson, M.R., Balding, D.J., 2012. Improved Heritability Estimation  
913 from Genome-wide SNPs. *Am. J. Hum. Genet.* 91, 1011–1021.  
914 <https://doi.org/10.1016/j.ajhg.2012.10.010>

915 Stamatakis, A., 2014. RAxML version 8: a tool for phylogenetic analysis and post-analysis of  
916 large phylogenies. *Bioinformatics* 30, 1312–1313.  
917 <https://doi.org/10.1093/bioinformatics/btu033>

918 Steenkamp, E.T., Wingfield, M.J., McTaggart, A.R., Wingfield, B.D., 2018. Fungal species  
919 and their boundaries matter – Definitions, mechanisms and practical implications.  
920 *Fungal Biol. Rev.* 32, 104–116. <https://doi.org/10.1016/j.fbr.2017.11.002>

921 Stukenbrock, E.H., 2016. The Role of Hybridization in the Evolution and Emergence of New  
922 Fungal Plant Pathogens. *Phytopathology* 106, 104–112.  
923 <https://doi.org/10.1094/PHYTO-08-15-0184-RVW>

924 Suzuki, R., Shimodaira, H., 2006. Pvcust: an R package for assessing the uncertainty in  
925 hierarchical clustering. *Bioinformatics* 22, 1540–1542.  
926 <https://doi.org/10.1093/bioinformatics/btl117>

927 Tajima, F., 1989. Statistical Method for Testing the Neutral Mutation Hypothesis by DNA  
928 Polymorphism. *Genetics* 123, 585–595.

929 Taylor, D.J., Hebert, P.D., 1993. Habitat-dependent hybrid parentage and differential  
930 introgression between neighboringly sympatric *Daphnia* species. *Proc. Natl. Acad. Sci.*  
931 90, 7079–7083. <https://doi.org/10.1073/pnas.90.15.7079>

932 Team, R.C., 2014. R: A language and environment for statistical computing.

933 Teresa Avelar, A., Perfeito, L., Gordo, I., Godinho Ferreira, M., 2013. Genome architecture is  
934 a selectable trait that can be maintained by antagonistic pleiotropy. *Nat. Commun.* 4,  
935 2235. <https://doi.org/10.1038/ncomms3235>

936 The Heliconius Genome Consortium, Dasmahapatra, K.K., Walters, J.R., Briscoe, A.D.,  
937 Davey, J.W., Whibley, A., Nadeau, N.J., Zimin, A.V., Hughes, D.S.T., Ferguson, L.C.,  
938 Martin, S.H., Salazar, C., Lewis, J.J., Adler, S., Ahn, S.-J., Baker, D.A., Baxter, S.W.,  
939 Chamberlain, N.L., Chauhan, R., Counterman, B.A., Dalmay, T., Gilbert, L.E.,  
940 Gordon, K., Heckel, D.G., Hines, H.M., Hoff, K.J., Holland, P.W.H., Jacquin-Joly, E.,  
941 Jiggins, F.M., Jones, R.T., Kapan, D.D., Kersey, P., Lamas, G., Lawson, D., Mapleson,  
942 D., Maroja, L.S., Martin, A., Moxon, S., Palmer, W.J., Papa, R., Papanicolaou, A.,  
943 Pauchet, Y., Ray, D.A., Rosser, N., Salzberg, S.L., Supple, M.A., Surridge, A.,  
944 Tenger-Trolander, A., Vogel, H., Wilkinson, P.A., Wilson, D., Yorke, J.A., Yuan, F.,  
945 Balmuth, A.L., Eland, C., Gharbi, K., Thomson, M., Gibbs, R.A., Han, Y., Jayaseelan,  
946 J.C., Kovar, C., Mathew, T., Muzny, D.M., Onger, F., Pu, L.-L., Qu, J., Thornton,  
947 R.L., Worley, K.C., Wu, Y.-Q., Linares, M., Blaxter, M.L., French-Constant, R.H.,  
948 Joron, M., Kronforst, M.R., Mullen, S.P., Reed, R.D., Scherer, S.E., Richards, S.,  
949 Mallet, J., Owen McMillan, W., Jiggins, C.D., 2012. Butterfly genome reveals  
950 promiscuous exchange of mimicry adaptations among species. *Nature* 487, 94–98.  
951 <https://doi.org/10.1038/nature11041>

952 Turner, L.M., Harr, B., 2014. Genome-wide mapping in a house mouse hybrid zone reveals  
953 hybrid sterility loci and Dobzhansky-Muller interactions. *eLife* 3, e02504.  
954 <https://doi.org/10.7554/eLife.02504>

955 Twyford, A.D., Streisfeld, M.A., Lowry, D.B., Friedman, J., 2015. Genomic studies on the  
956 nature of species: adaptation and speciation in *Mimulus*. *Mol. Ecol.* 24, 2601–2609.  
957 <https://doi.org/10.1111/mec.13190>

958 Vijay, N., Bossu, C.M., Poelstra, J.W., Weissensteiner, M.H., Suh, A., Kryukov, A.P., Wolf,  
959 J.B.W., 2016. Evolution of heterogeneous genome differentiation across multiple  
960 contact zones in a crow species complex. *Nat. Commun.* 7, 13195.  
961 <https://doi.org/10.1038/ncomms13195>

962 Walker, B.J., Abeel, T., Shea, T., Priest, M., Abouelliel, A., Sakthikumar, S., Cuomo, C.A.,  
963 Zeng, Q., Wortman, J., Young, S.K., Earl, A.M., 2014. Pilon: An Integrated Tool for  
964 Comprehensive Microbial Variant Detection and Genome Assembly Improvement.  
965 *PLoS ONE* 9, e112963. <https://doi.org/10.1371/journal.pone.0112963>

966 Watterson, G.A., 1975. On the number of segregating sites in genetical models without  
967 recombination. *Theor. Popul. Biol.* 7, 256–276. [https://doi.org/10.1016/0040-5809\(75\)90020-9](https://doi.org/10.1016/0040-5809(75)90020-9)

968

969 Weir, B.S., 1979. Inferences about Linkage Disequilibrium. *Biometrics* 35, 235.  
970 <https://doi.org/10.2307/2529947>

971 Wellenreuther, M., Bernatchez, L., 2018. Eco-Evolutionary Genomics of Chromosomal  
972 Inversions. *Trends Ecol. Evol.* 33, 427–440. <https://doi.org/10.1016/j.tree.2018.04.002>

973 Wood, V., Gwilliam, R., Rajandream, M.-A., Lyne, M., Lyne, R., Stewart, A., Sgouros, J.,  
974 Peat, N., Hayles, J., Baker, S., Basham, D., Bowman, S., Brooks, K., Brown, D.,  
975 Brown, S., Chillingworth, T., Churcher, C., Collins, M., Connor, R., Cronin, A., Davis,  
976 P., Feltwell, T., Fraser, A., Gentles, S., Goble, A., Hamlin, N., Harris, D., Hidalgo, J.,  
977 Hodgson, G., Holroyd, S., Hornsby, T., Howarth, S., Huckle, E.J., Hunt, S., Jagels, K.,  
978 James, K., Jones, L., Jones, M., Leather, S., McDonald, S., McLean, J., Mooney, P.,  
979 Moule, S., Mungall, K., Murphy, L., Niblett, D., Odell, C., Oliver, K., O’Neil, S.,  
980 Pearson, D., Quail, M.A., Rabinowitsch, E., Rutherford, K., Rutter, S., Saunders, D.,  
981 Seeger, K., Sharp, S., Skelton, J., Simmonds, M., Squares, R., Squares, S., Stevens, K.,  
982 Taylor, K., Taylor, R.G., Tivey, A., Walsh, S., Warren, T., Whitehead, S., Woodward,  
983 J., Volckaert, G., Aert, R., Robben, J., Grymonprez, B., Weltjens, I., Vanstreels, E.,  
984 Rieger, M., Schäfer, M., Müller-Auer, S., Gabel, C., Fuchs, M., Dusterhöft, A., Fritze,  
985 C., Holzer, E., Moestl, D., Hilbert, H., Borzým, K., Langer, I., Beck, A., Lehrach, H.,

986 Reinhardt, R., Pohl, T.M., Eger, P., Zimmermann, W., Wedler, H., Wambutt, R.,  
 987 Purnelle, B., Goffeau, A., Cadieu, E., Dréano, S., Gloux, S., Lelaure, V., Mottier, S.,  
 988 Galibert, F., Aves, S.J., Xiang, Z., Hunt, C., Moore, K., Hurst, S.M., Lucas, M.,  
 989 Rochet, M., Gaillardin, C., Tallada, V.A., Garzon, A., Thode, G., Daga, R.R., Cruzado,  
 990 L., Jimenez, J., Sánchez, M., del Rey, F., Benito, J., Domínguez, A., Revuelta, J.L.,  
 991 Moreno, S., Armstrong, J., Forsburg, S.L., Cerutti, L., Lowe, T., McCombie, W.R.,  
 992 Paulsen, I., Potashkin, J., Shpakovski, G.V., Ussery, D., Barrell, B.G., Nurse, P., 2003.  
 993 Erratum: corrigendum: The genome sequence of *Schizosaccharomyces pombe*. *Nature*  
 994 421, 94–94. <https://doi.org/10.1038/nature01203>  
 995 Wood, V., Gwilliam, R., Rajandream, M.-A., Lyne, M., Lyne, R., Stewart, A., Sgouros, J.,  
 996 Peat, N., Hayles, J., Baker, S., Basham, D., Bowman, S., Brooks, K., Brown, D.,  
 997 Brown, S., Chillingworth, T., Churcher, C., Collins, M., Connor, R., Cronin, A., Davis,  
 998 P., Feltwell, T., Fraser, A., Gentles, S., Goble, A., Hamlin, N., Harris, D., Hidalgo, J.,  
 999 Hodgson, G., Holroyd, S., Hornsby, T., Howarth, S., Huckle, E.J., Hunt, S., Jagels, K.,  
 1000 James, K., Jones, L., Jones, M., Leather, S., McDonald, S., McLean, J., Mooney, P.,  
 1001 Moule, S., Mungall, K., Murphy, L., Niblett, D., Odell, C., Oliver, K., O’Neil, S.,  
 1002 Pearson, D., Quail, M.A., Rabinowitsch, E., Rutherford, K., Rutter, S., Saunders, D.,  
 1003 Seeger, K., Sharp, S., Skelton, J., Simmonds, M., Squares, R., Squares, S., Stevens, K.,  
 1004 Taylor, K., Taylor, R.G., Tivey, A., Walsh, S., Warren, T., Whitehead, S., Woodward,  
 1005 J., Volckaert, G., Aert, R., Robben, J., Grymonprez, B., Weltjens, I., Vanstreels, E.,  
 1006 Rieger, M., Schäfer, M., Müller-Auer, S., Gabel, C., Fuchs, M., Fritzc, C., Holzer, E.,  
 1007 Moestl, D., Hilbert, H., Borzym, K., Langer, I., Beck, A., Lehrach, H., Reinhardt, R.,  
 1008 Pohl, T.M., Eger, P., Zimmermann, W., Wedler, H., Wambutt, R., Purnelle, B.,  
 1009 Goffeau, A., Cadieu, E., Dréano, S., Gloux, S., Lelaure, V., Mottier, S., Galibert, F.,  
 1010 Aves, S.J., Xiang, Z., Hunt, C., Moore, K., Hurst, S.M., Lucas, M., Rochet, M.,  
 1011 Gaillardin, C., Tallada, V.A., Garzon, A., Thode, G., Daga, R.R., Cruzado, L.,  
 1012 Jimenez, J., Sánchez, M., del Rey, F., Benito, J., Domínguez, A., Revuelta, J.L.,  
 1013 Moreno, S., Armstrong, J., Forsburg, S.L., Cerrutti, L., Lowe, T., McCombie, W.R.,  
 1014 Paulsen, I., Potashkin, J., Shpakovski, G.V., Ussery, D., Barrell, B.G., Nurse, P., 2002.  
 1015 Erratum: The genome sequence of *Schizosaccharomyces pombe*. *Nature* 415, 871–880.  
 1016 <https://doi.org/10.1038/nature724>  
 1017 Zanders, S.E., Eickbush, M.T., Yu, J.S., Kang, J.-W., Fowler, K.R., Smith, G.R., Malik, H.S.,  
 1018 2014. Genome rearrangements and pervasive meiotic drive cause hybrid infertility in  
 1019 fission yeast. *eLife* 3, e02630. <https://doi.org/10.7554/eLife.02630>  
 1020 Zheng, X., Gogarten, S.M., Lawrence, M., Stilp, A., Conomos, M.P., Weir, B.S., Laurie, C.,  
 1021 Levine, D., 2017. SeqArray—a storage-efficient high-performance data format for  
 1022 WGS variant calls. *Bioinformatics* 33, 2251–2257.  
 1023 <https://doi.org/10.1093/bioinformatics/btx145>  
 1024 Zheng, X., Levine, D., Shen, J., Gogarten, S.M., Laurie, C., Weir, B.S., 2012. A high-  
 1025 performance computing toolset for relatedness and principal component analysis of  
 1026 SNP data. *Bioinformatics* 28, 3326–3328.  
 1027 <https://doi.org/10.1093/bioinformatics/bts606>  
 1028  
 1029  
 1030  
 1031  
 1032  
 1033

1034 **Figure legends**

1035

1036 **Figure 1 | Distribution of *Sp* (red) and *Sk* (blue) ancestry blocks along the *S. pombe* genome.** (a)  
1037 Example of principal component analysis (PCA) of a representative genomic window in chromosome  
1038 I (top) and the whole mitochondrial DNA (bottom). Samples fall into two major clades, *Sp* (red  
1039 square) and *Sk* (blue square). The proportion of variance explained by PC1 and PC2 is indicated on the  
1040 axis labels. Additional examples are found in Supplementary Figure 1 (b) Proportion of variance  
1041 explained by PC1 (black line) and PC2 (grey line) for each genomic window along the genome.  
1042 Centromeres are indicated with red bars. Note the drop in proximity to centromeres and telomeres  
1043 where genotype quality is significantly reduced. (c) Heatmap for one representative of 57 near-clonal  
1044 groups indicating ancestry along the genome (right panel). Samples are organised according to a  
1045 hierarchical clustering, grouping samples based on ancestral block distribution (left dendrogram).  
1046 Colours on the tips of the cladogram represent cluster membership by chromosome (see  
1047 **Supplementary Figure 9**). Samples changing clustering group between chromosomes are shown in  
1048 grey. (d) Estimate of  $D_{xy}$  between ancestral groups and genetic diversity ( $\pi$ ) within the *Sp* (red) and *Sk*  
1049 clade (blue) along the genome.

1050

1051 **Figure 2 | Population genetic summary statistics.** (a) Proportion of *Sp* (red) and *Sk* (blue) ancestry  
1052 across all 57 samples along the genome. (b) Tajima's D differentiated by *Sp* (red) and *Sk* (blue)  
1053 ancestry and pooled across all samples irrespective of ancestry (grey line). Genomic regions  
1054 previously identified under purifying selection (Fawcett et al., 2014) are shown with black triangles.  
1055 Reported active meiotic drives (Zanders et al., 2014; Hu et al., 2017; Nuckolls et al., 2017) are  
1056 indicated by yellow triangles. The third panel shows the difference between ancestry specific Tajima's  
1057 D and the estimate from the pooled samples.

1058

1059 **Figure 3 | Inferred evolutionary history of contemporary *S. pombe* strains.** An ancestral  
1060 population diverged into two major clades, *Sp* (red) and *Sk* (blue) since approximately 2300 years ago  
1061 (Jeffares et al., 2015). Recurrent hybridization upon secondary contact initiated around 20-60 sexual  
1062 outcrossing generations ago resulted in admixed genomes with a range of admixture proportions  
1063 (bottom) prevailing today.

1064

1065 **Figure 4 | Ancestry explains variation in phenotype and reproductive isolation.** (a) PCA of  
1066 normalized phenotypic variation across 228 traits. The proportion of variance explained by PC1 and  
1067 PC2 is indicated on the axis labels. Admixed samples (dots) are coloured coded by ancestry proportion  
1068 (cf. **Figure 3**) ranging from pure *Sp* (red triangle) to pure *Sk* (blue triangle) ancestry. (b) Phenotypic  
1069 distribution of example traits separated by the degree of admixture: admixed samples are shown in  
1070 grey, pure ancestral *Sp* and *Sk* samples are shown in red and blue respectively. The number of traits

1071 corresponding to a dominant, additive and transgressive genetic architecture is indicated on the right  
1072 hand side (c) Comparison of heritability estimates of all 228 traits based on 172,935 SNPs (abscissa)  
1073 and on 1925 genomic windows polarized by ancestry (ordinate). Colours indicate statistical  
1074 significance. *NS*: heritability values not significantly different from zero, *AncHap*: significant only  
1075 using ancestral blocks, *SNPs*: significant only using SNPs, *SB*: significant in both analyses. Diagonal  
1076 (slope=1) added as reference. (d) Histogram of the difference between heritability estimates using  
1077 SNPs and ancestry components for all 228 traits. (e) Correlation between the difference in ancestry  
1078 proportions between two strains (cf. **Figure 2**) and spore viability of the cross. Red box shows samples  
1079 with low spore viability but high genetic similarity.

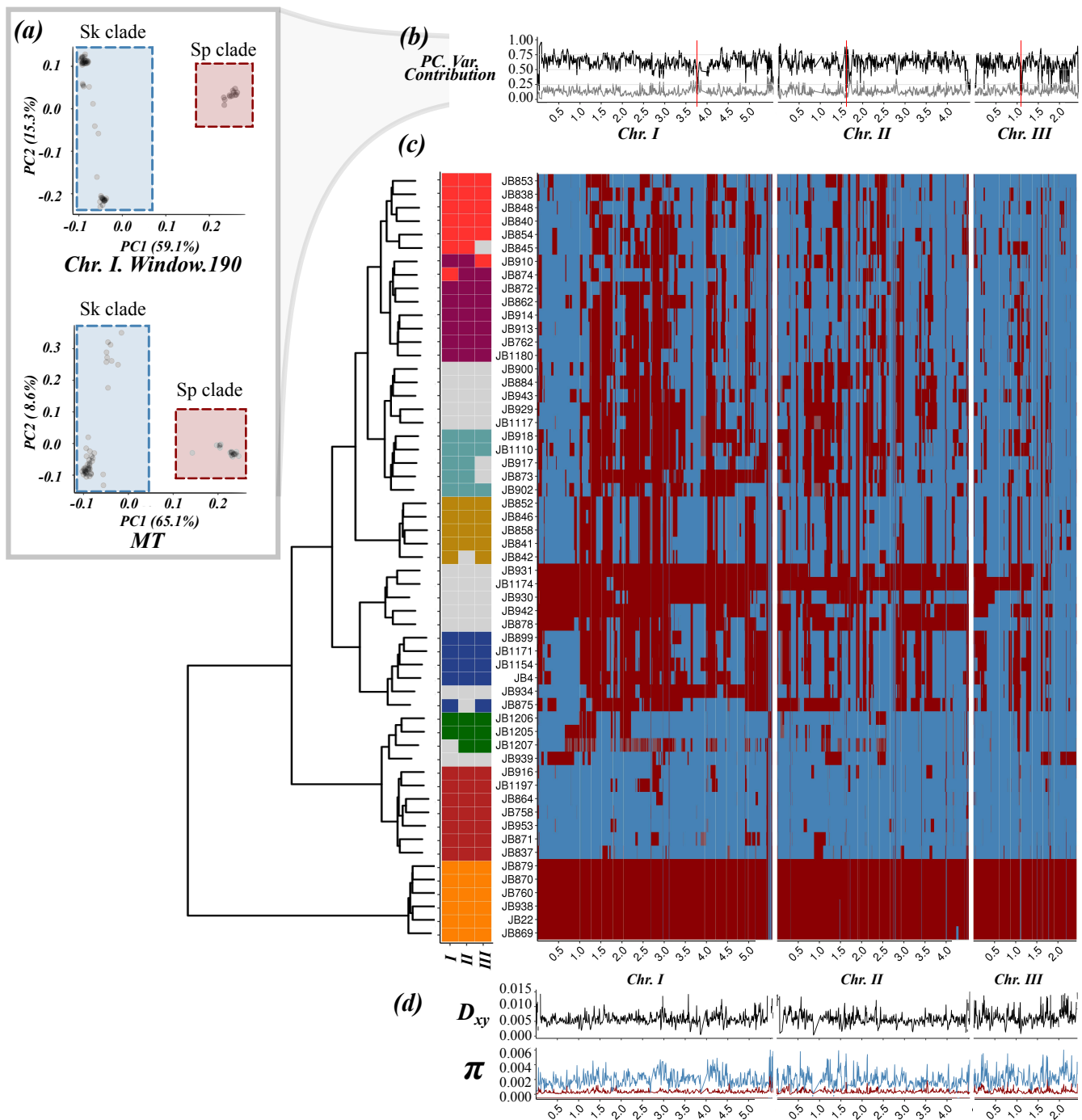
1080

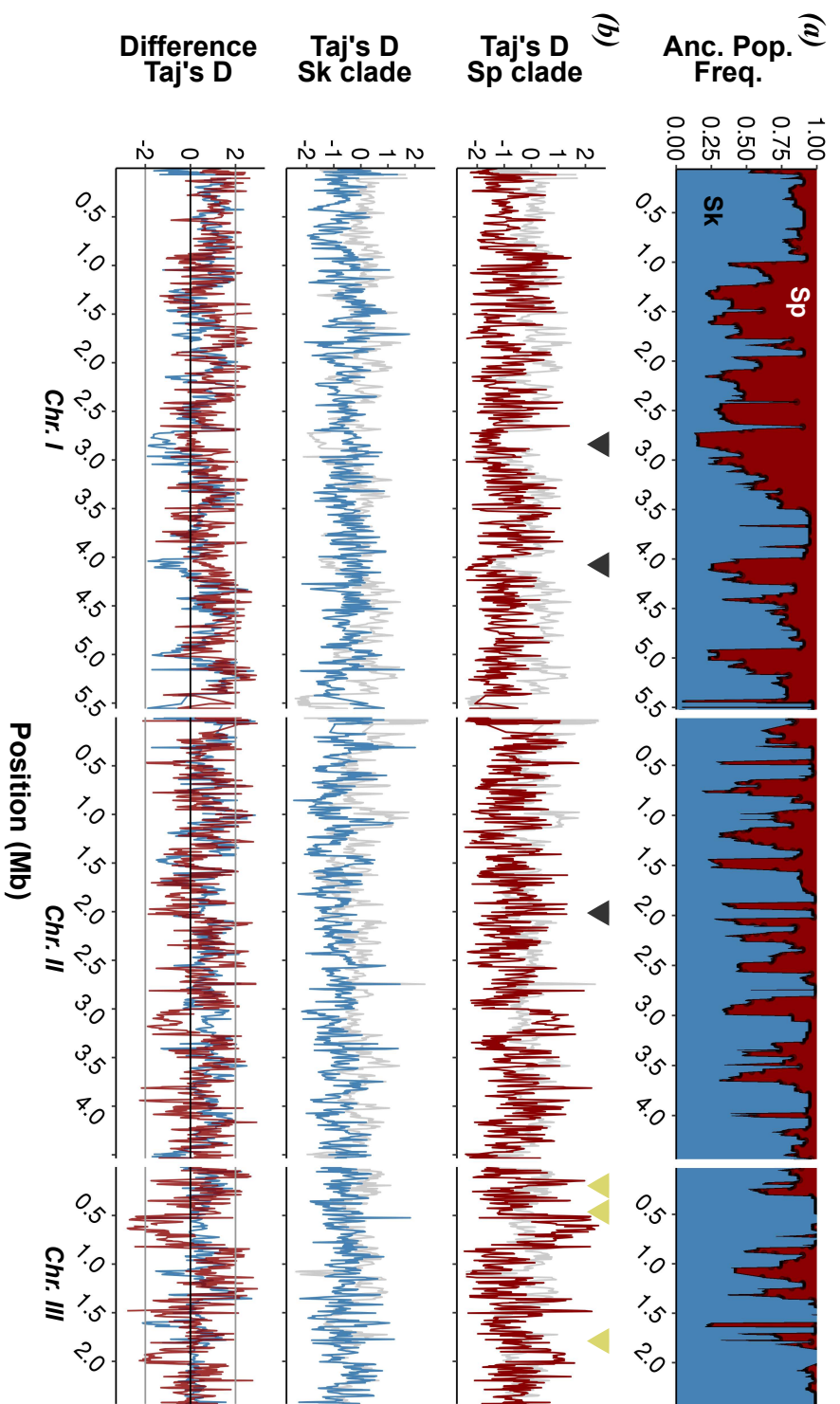
1081 **Figure 5 | Characterization of structural variation based on long-read, real-time sequencing.** (a)  
1082 Schematic representation of the three chromosomes in different strains displaying SVs larger than  
1083 10kb relative to reference genome JB22 (left panel). Chromosome arms are differentiated by colour;  
1084 orientation is indicated with arrows relative to the reference; black bars represent centromeres. In the  
1085 second panel, additional SVs, their type and ID of the corresponding strain are illustrated in brackets.  
1086 (b) Size distribution of SVs below 10 kb. Colours indicate the type of SV. (c) Distribution of SV  
1087 density along the genome. Black bars represent centromeres. (d) Two-dimensional, folded site  
1088 frequency spectrum between inferred ancestral populations for all SVs, SNPs and LTR INDELS.  
1089 Numbers and colours show the percentage of the total number of variants in each category. Variants  
1090 with low frequency in both populations are shown in the blue box. Variants highly differentiated  
1091 between populations are shown in red boxes with total in the upper right box. Fills with percentage  
1092 lower than 0.01 are empty.

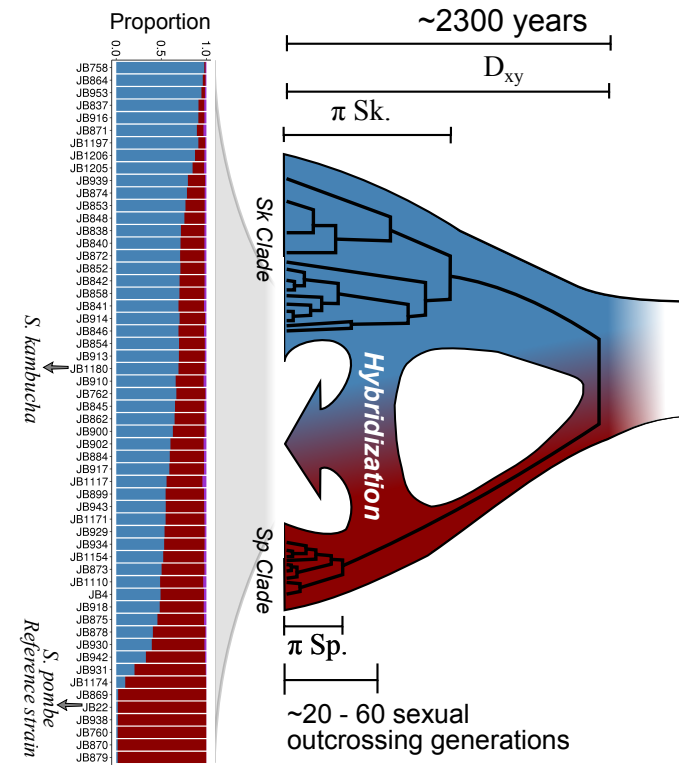
1093 *Abbreviations:* DEL: deletion; DUP: duplication; INS: insertion; INV: inversion

1094

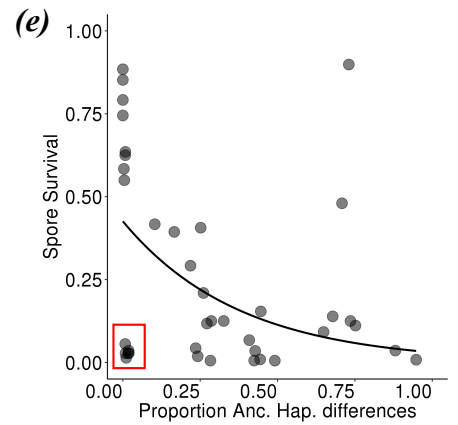
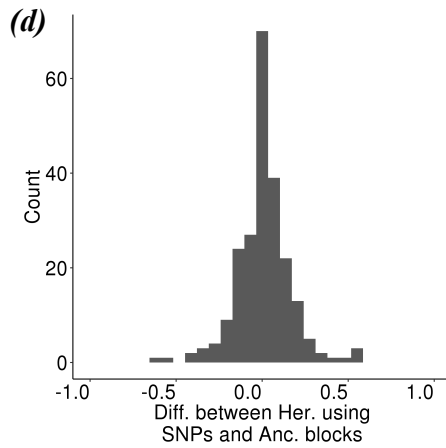
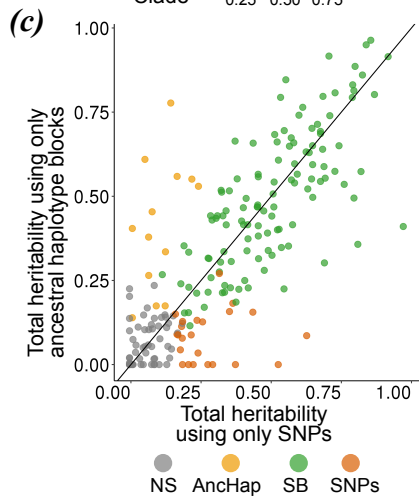
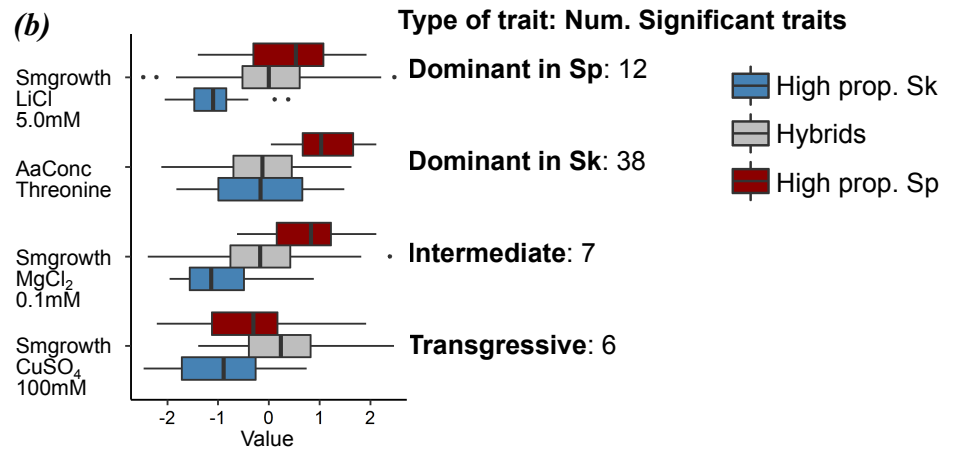
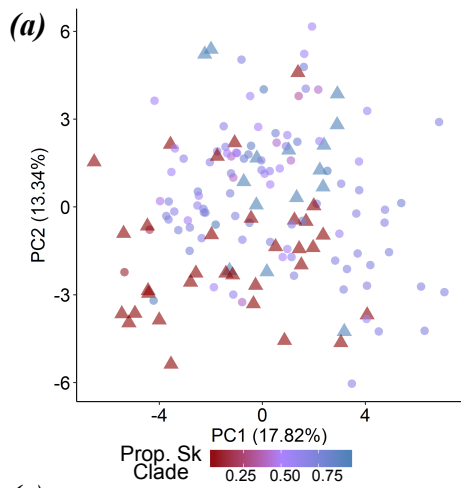
1095 **Figure 6 | Decay in linkage disequilibrium (LD) with genetic distance.** Relationship between LD  
1096 ( $R^2$ ) and physical distance is depicted for each chromosome. Black points represent values for each  
1097 window pair comparison. Lines show non-linear regression model based on Hill & Weir (1988) and  
1098 Remington et al. (2001). LD estimates were divided into three categories representing comparison  
1099 between windows of shared ancestry (*Sp-Sp* or *Sk-Sk*) reflecting positive ancestry disequilibrium (AD)  
1100 or of opposite ancestry (*Sk-Sp*) reflecting negative AD.



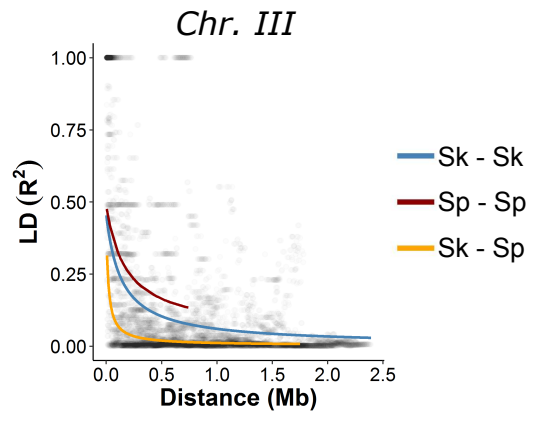
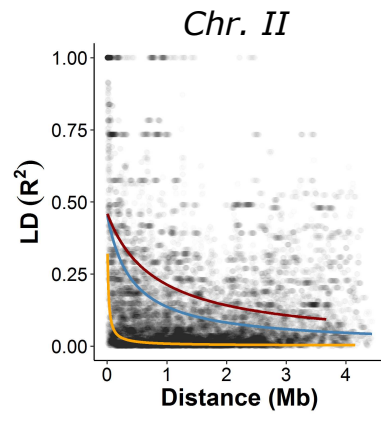
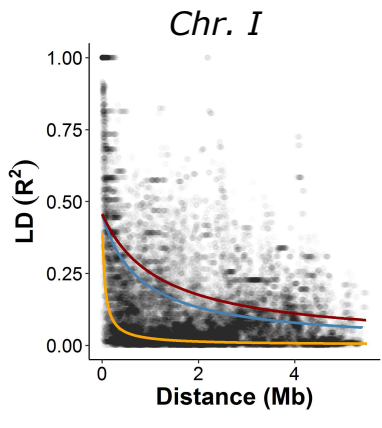




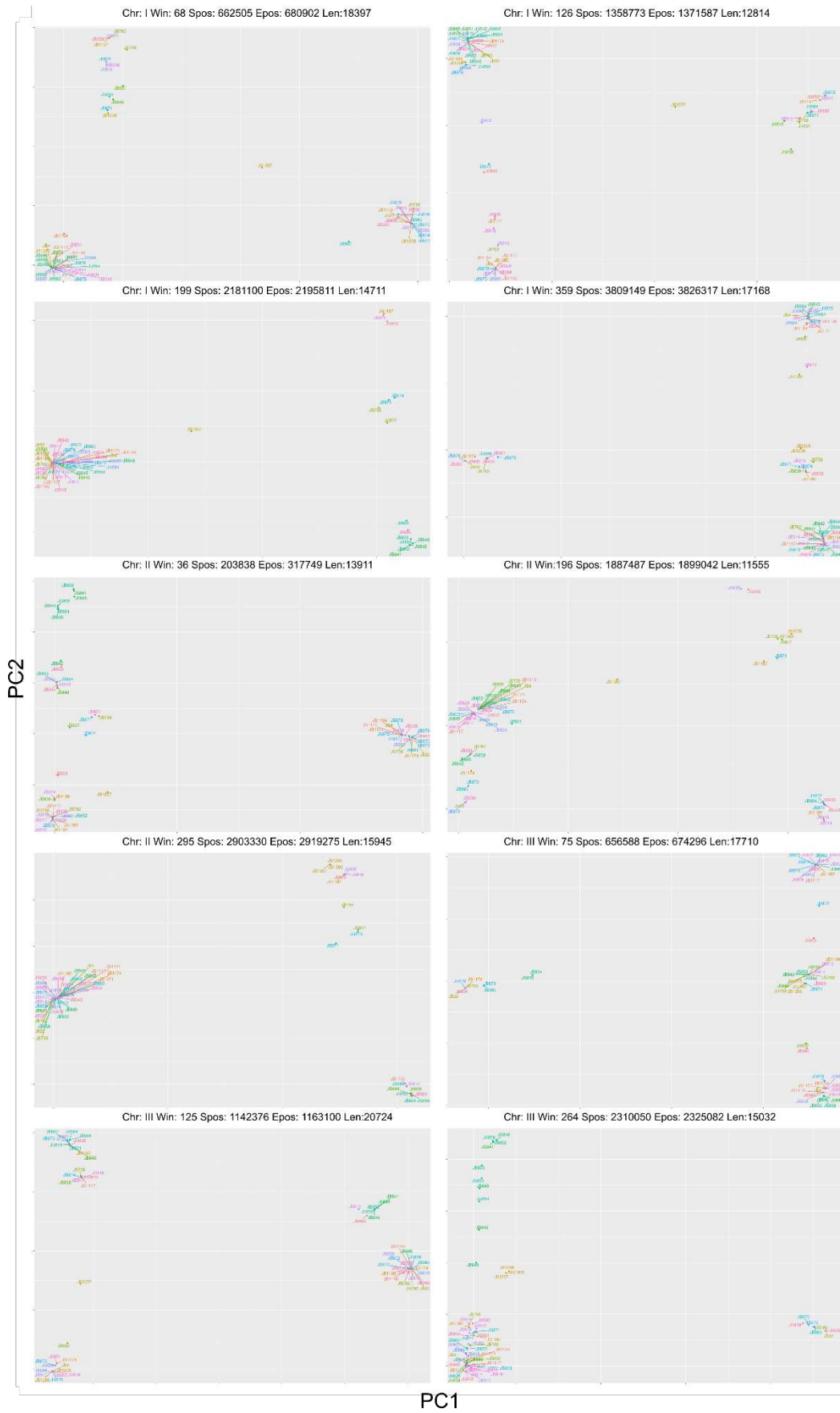




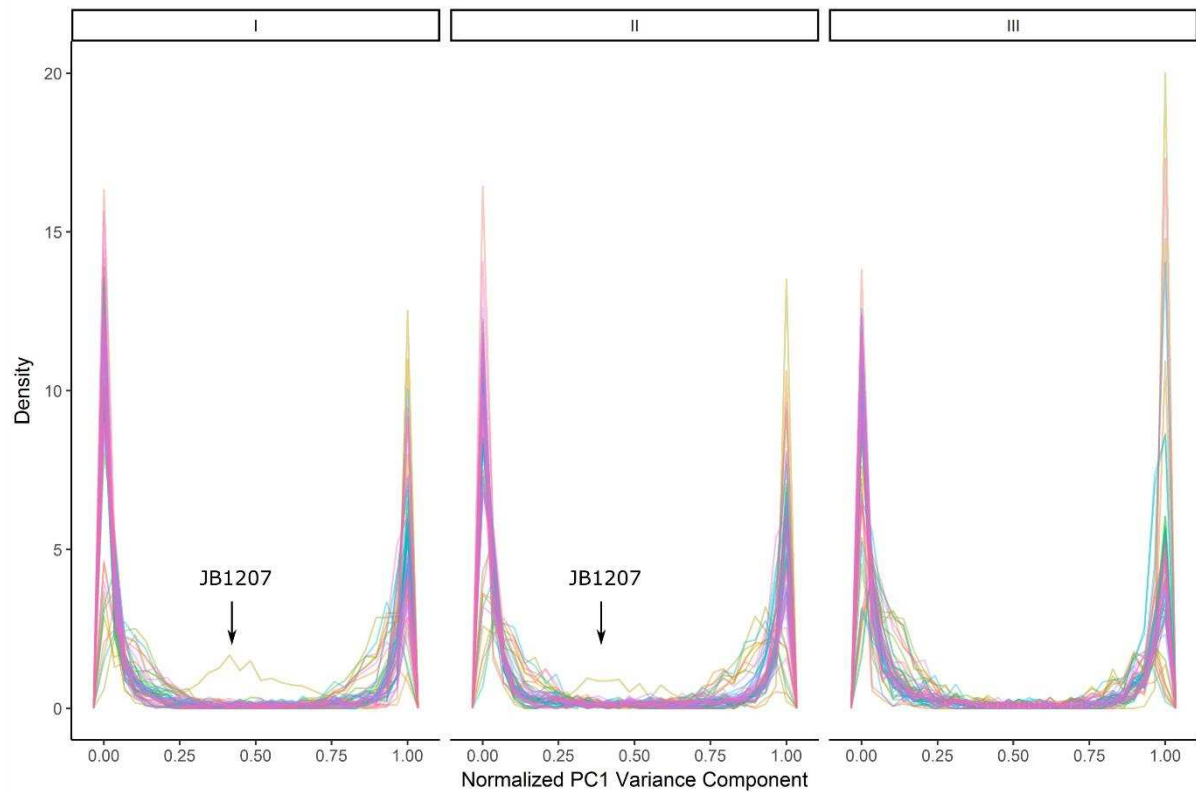




## Supplementary Figures



**Supplementary Figure 1: Example of principal component analysis (PCA).** Each panel is an example PCA of different genomic windows. The chromosome (Chr.), window number (Win), start and end position (Spos and Epos) and length of the window in bp (Len) are shown in the header for each panel. Samples are differentiated by colours.



**Supplementary Figure 2: Normalised PC1 distribution.** Density plot of Normalised PC1 values shown separately for each of the three chromosomes. Each line represent one sample. The sample JB1207 is highlighted as it is the only sample with a high proportion of intermediate values.

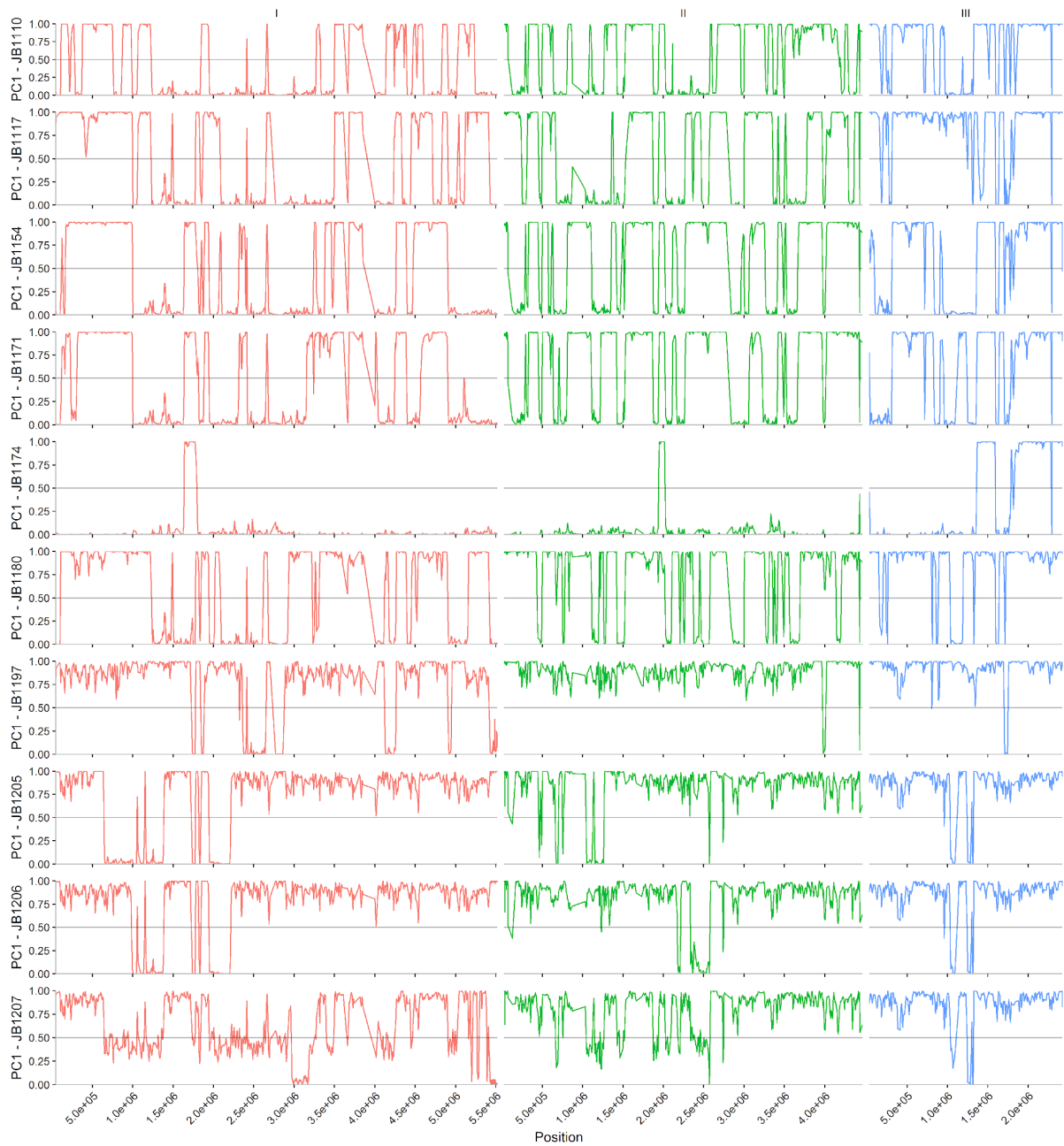


Figure continues on next page.

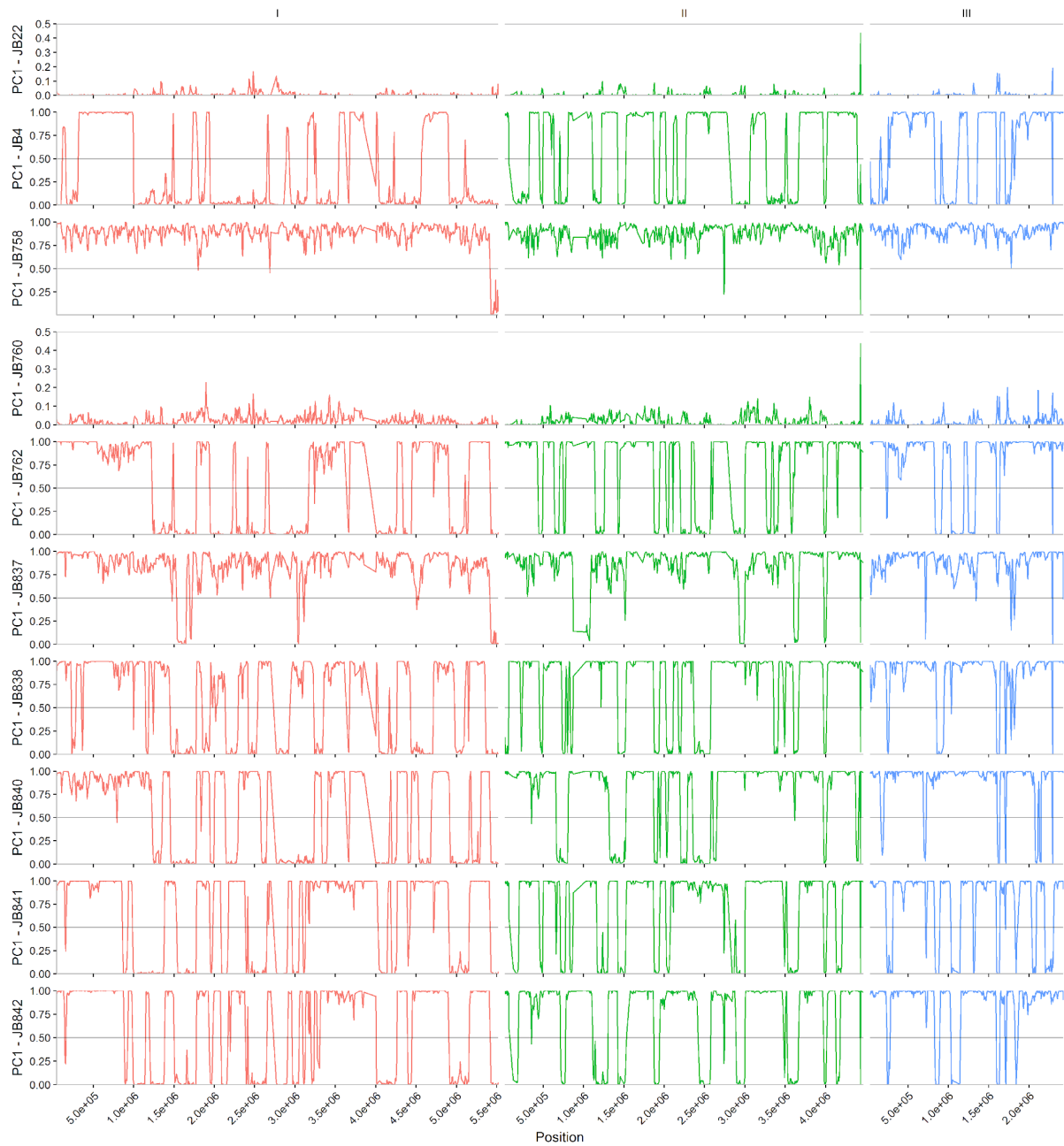


Figure continues on next page.



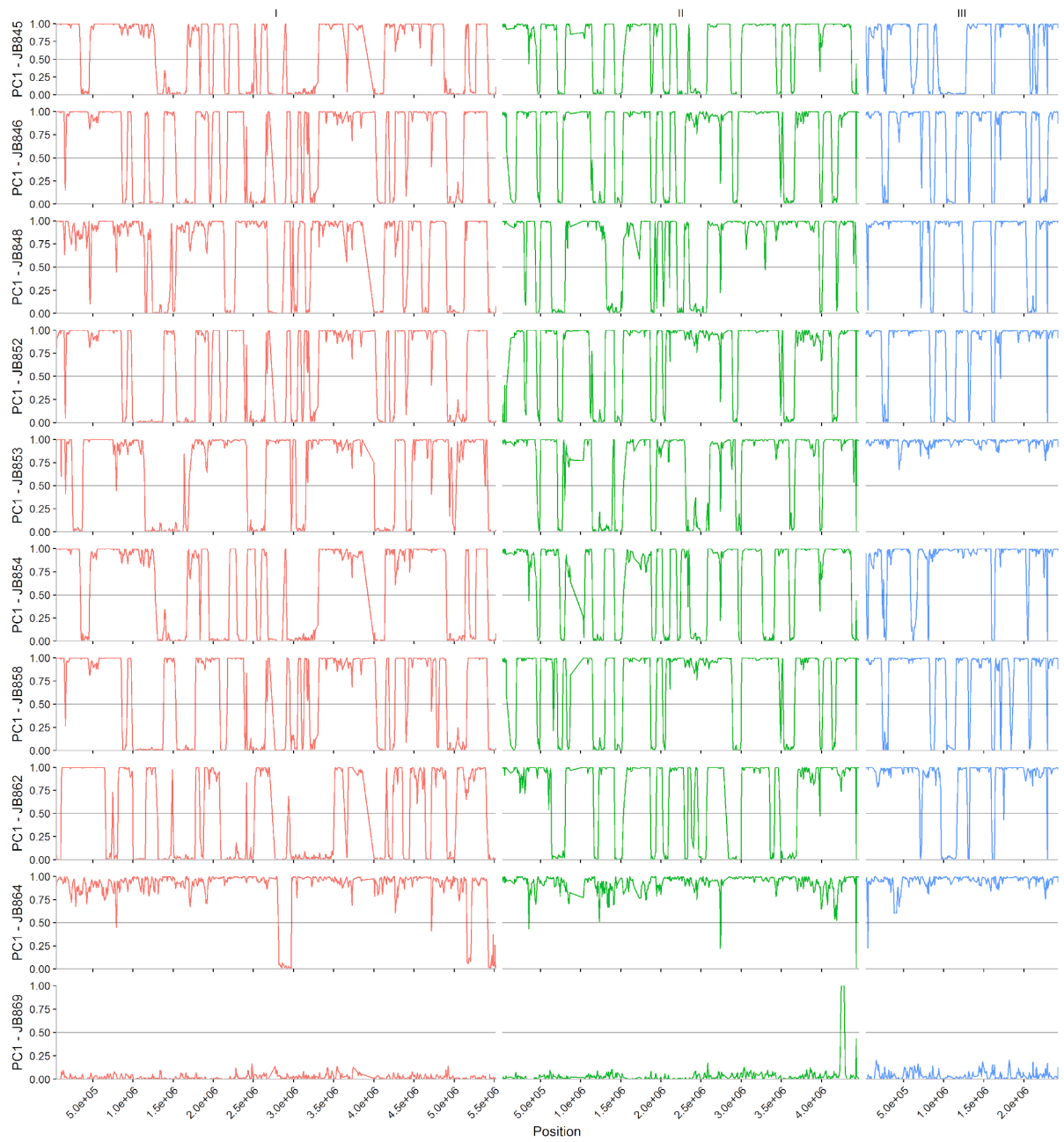


Figure continues on next page.

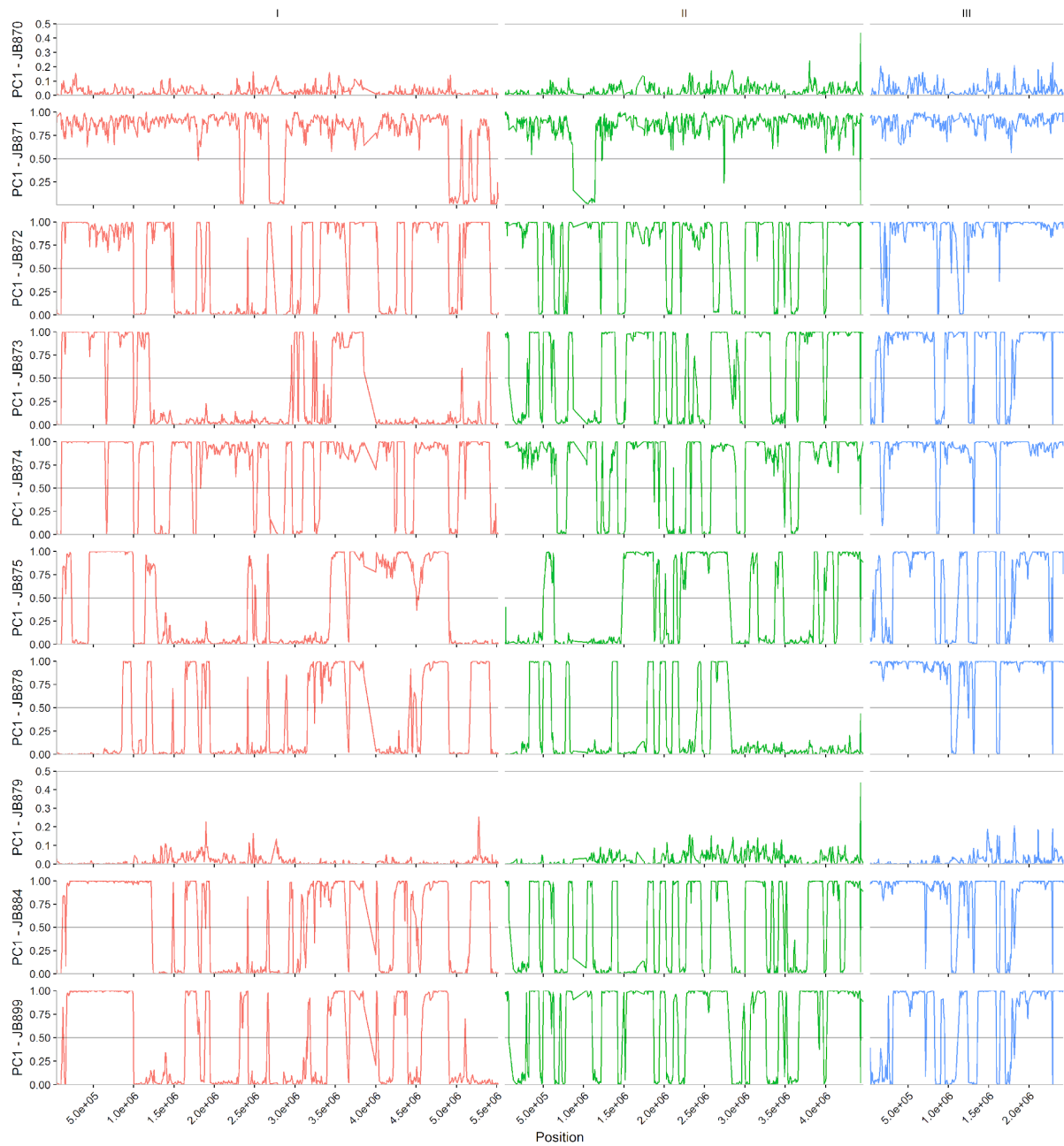


Figure continues on next page.

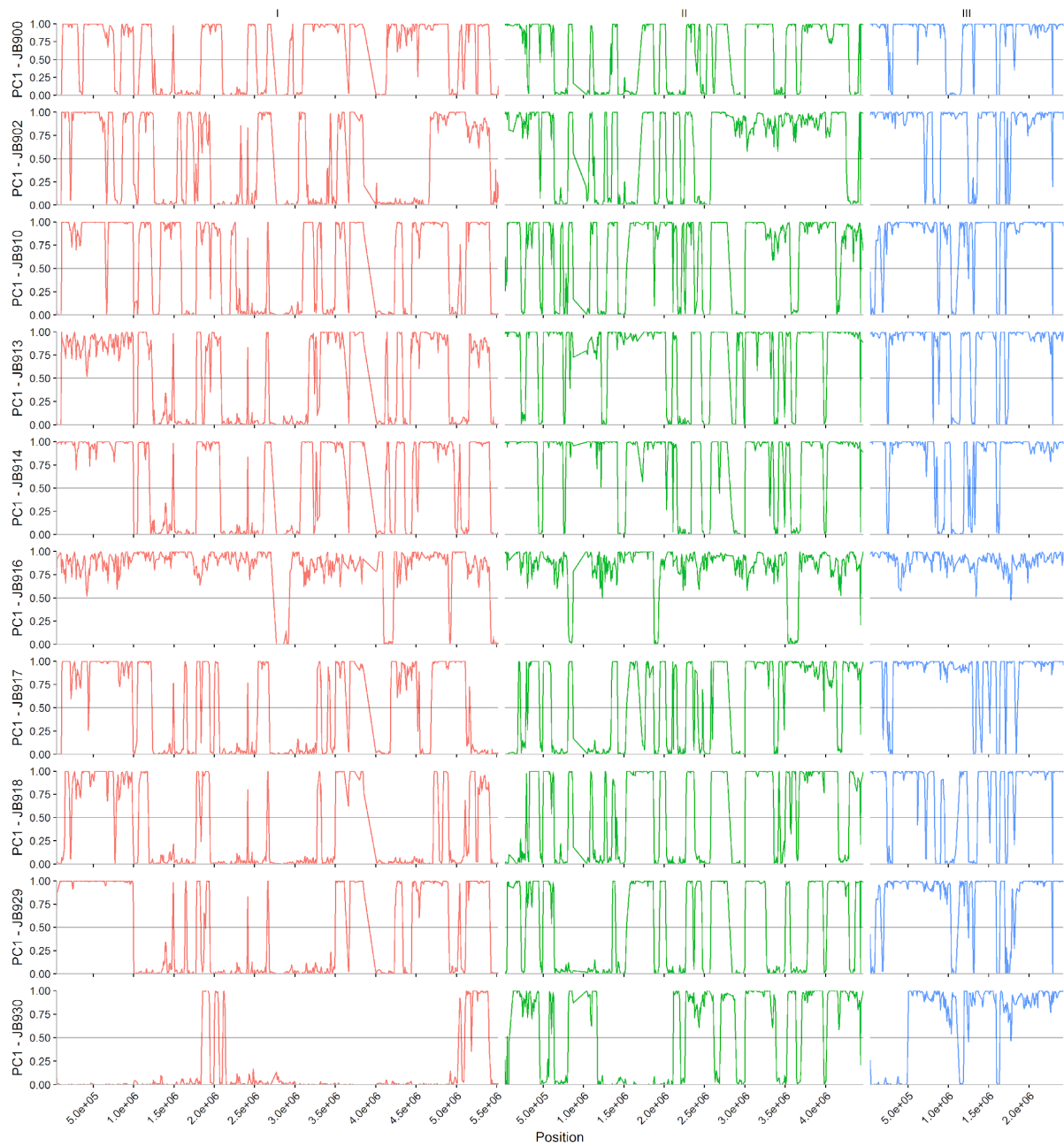
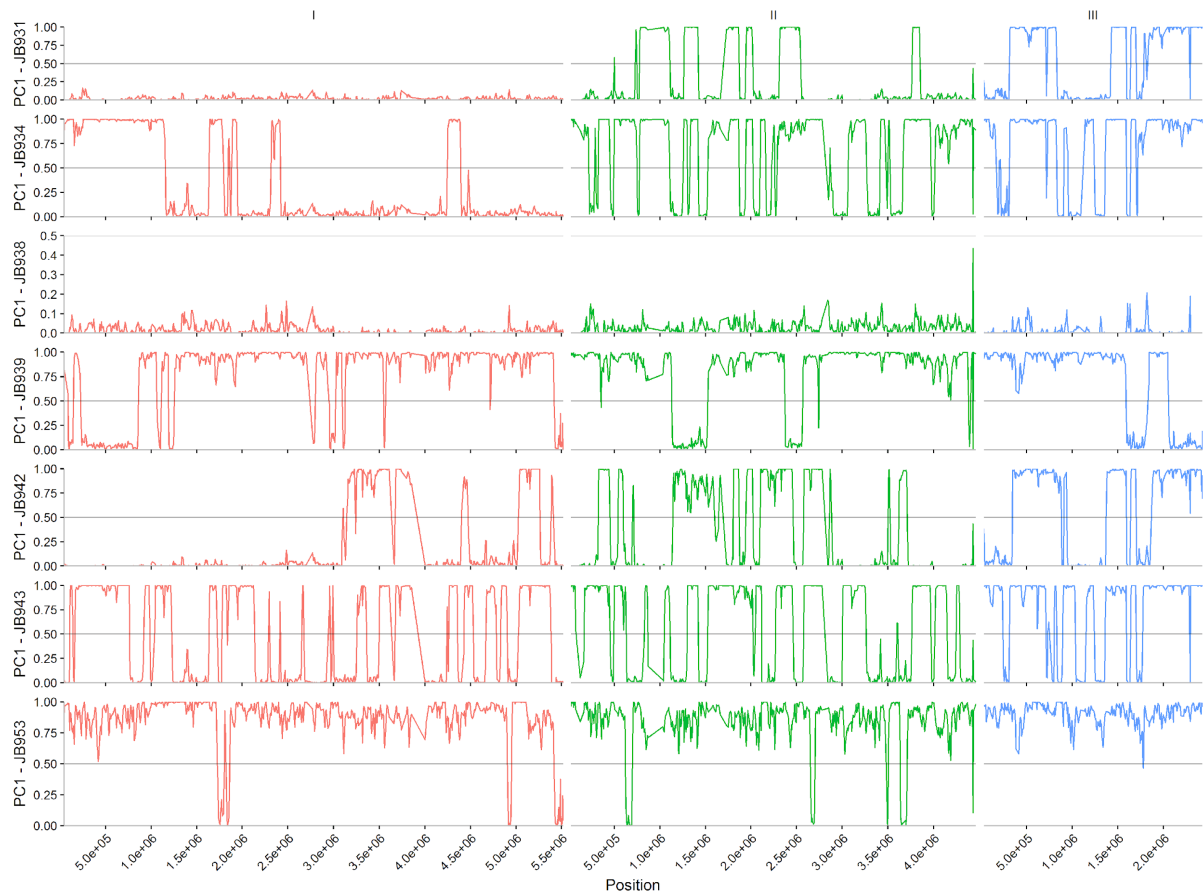
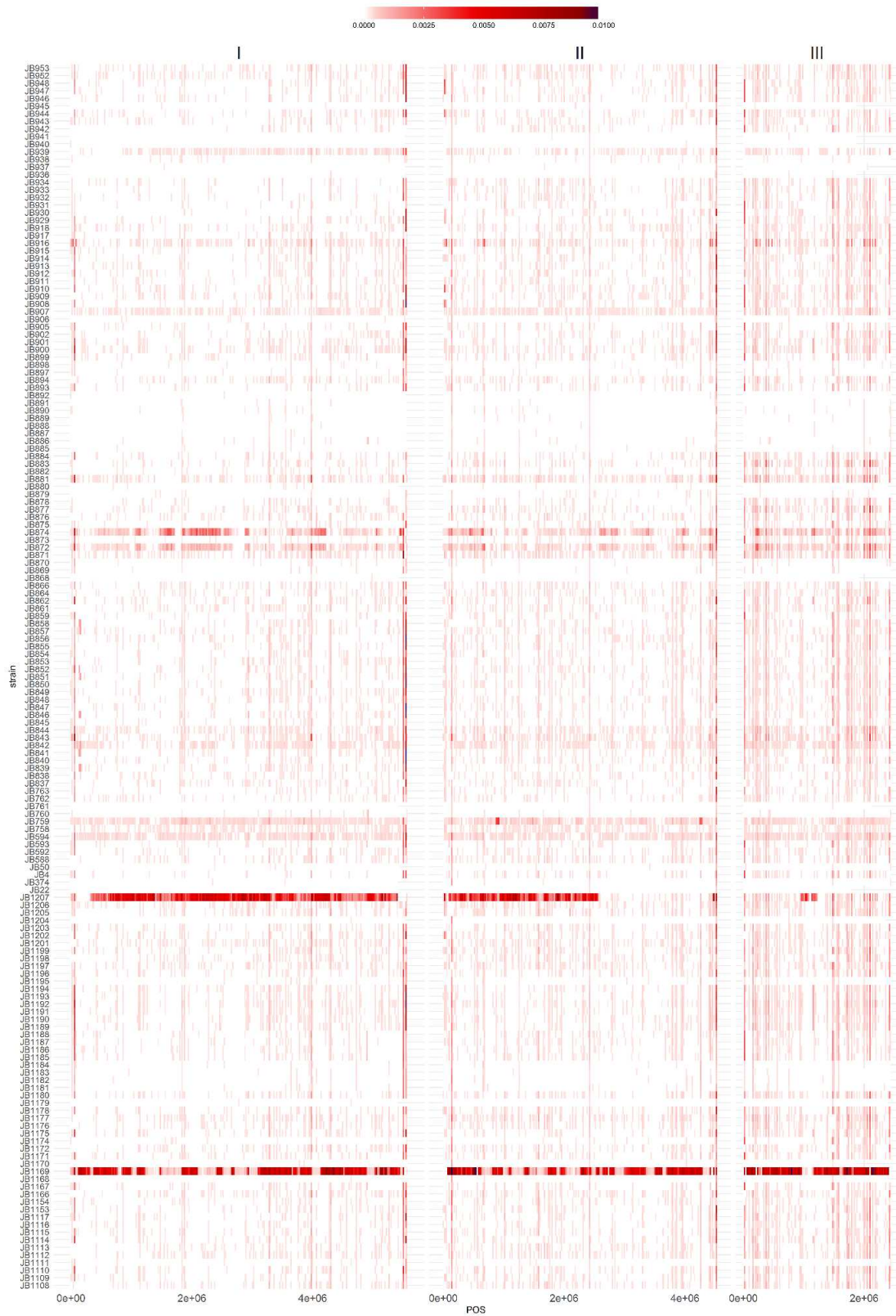


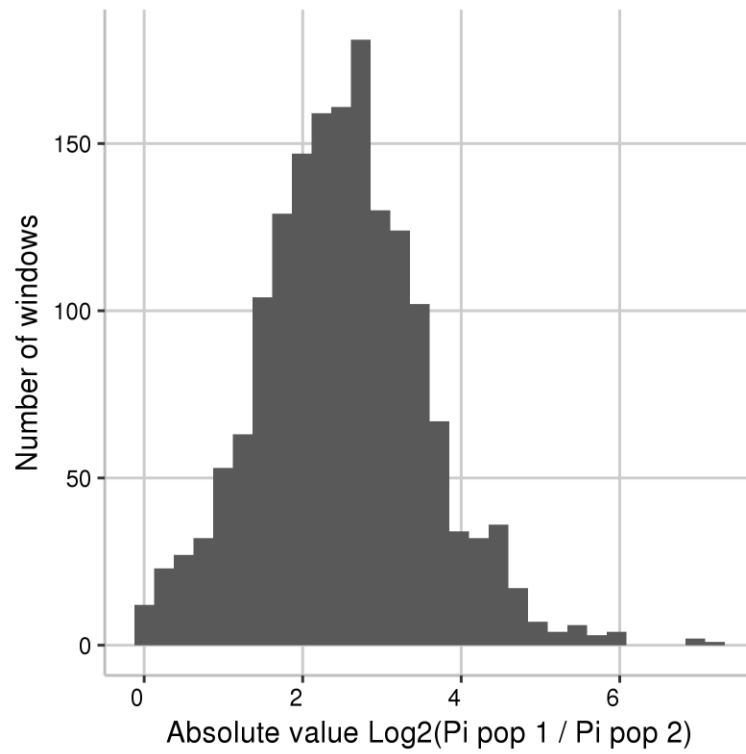
Figure continues on next page.



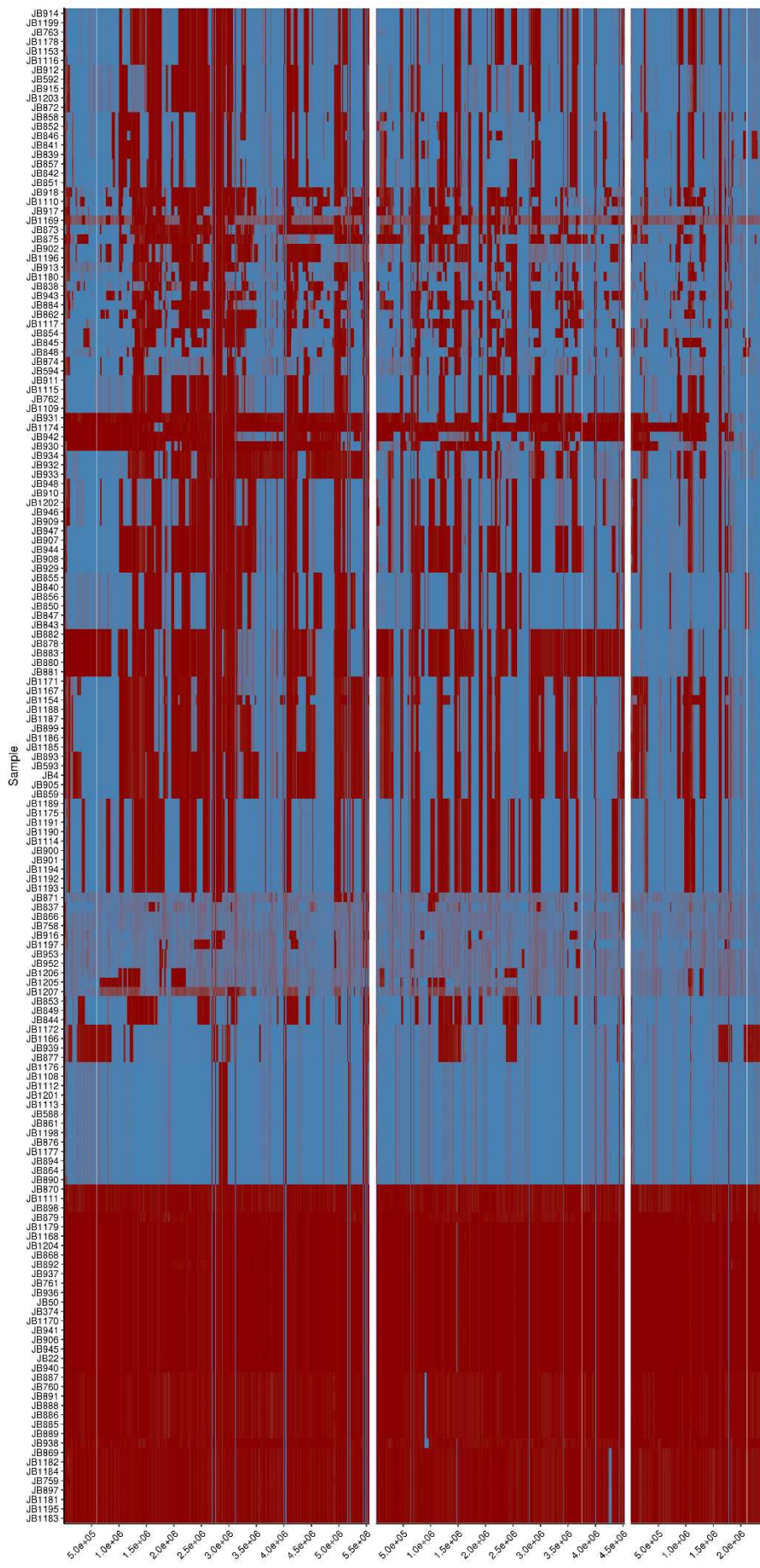
**Supplementary Figure 3: Distribution of normalised PC1 values along the genome.** Chromosomes are indicated by colour (chr1 = red; chr2 = green, chr3 = blue). Normalised PC1 values were polarized based on genetic diversity as described in the methods section, values close to 0 or 1 represent genomic regions with the *Sp* or *Sk* haplotype, respectively.



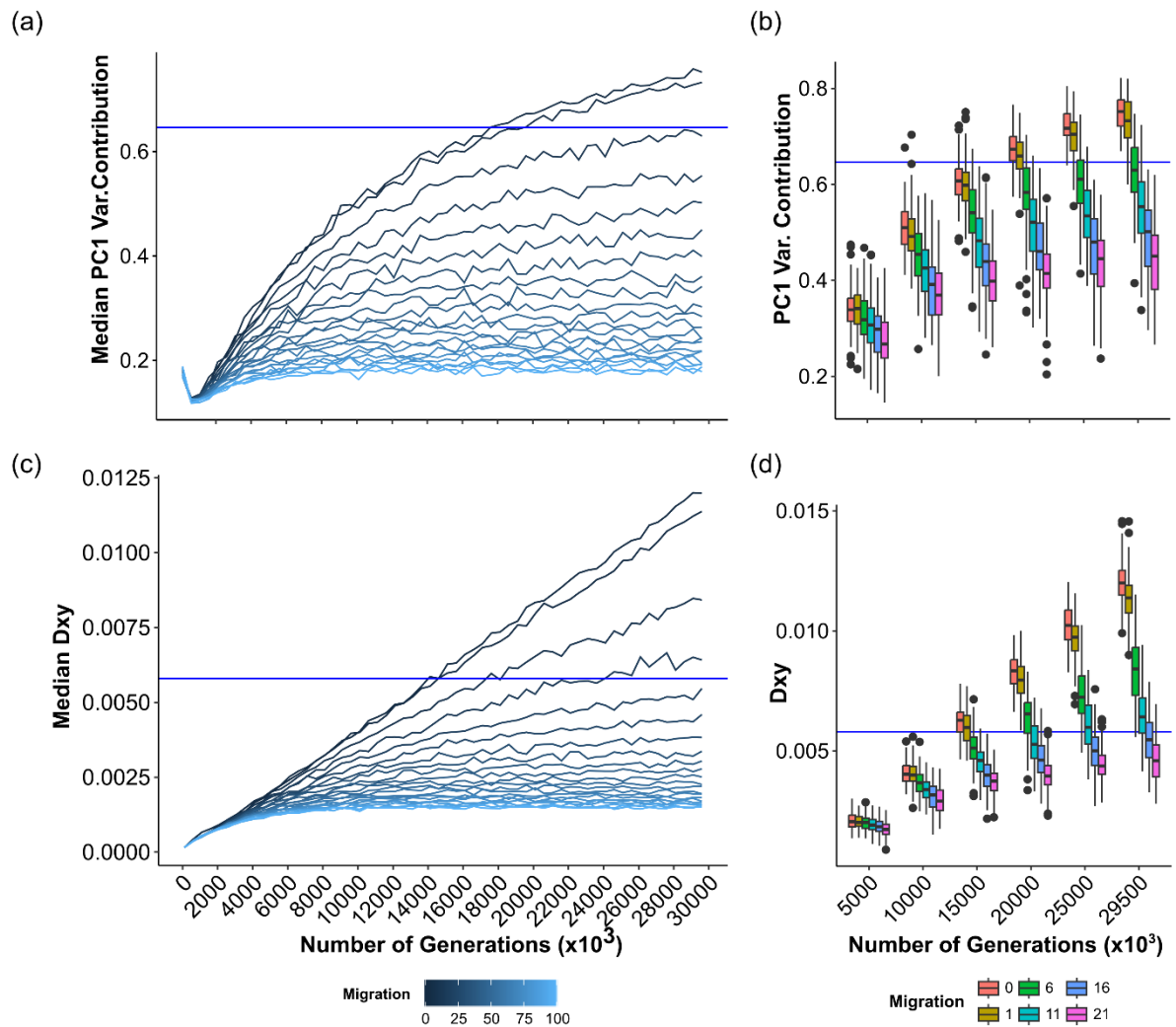
**Supplementary Figure 4: Heterozygosity along the genome.** Heatmap of heterozygosity per 20kb window and sample along the genome. High heterozygosity values are shown in red. Strains JB1207 and JB1169 show high heterozygosity along large parts of the genome.



**Supplementary Figure 5: Difference in genetic diversity between ancestral groups.** Histogram of the ratio in genetic diversity ( $\pi$ ) between the ancestral clade *Sk* over the *Sp* clade. Note that values are presented on a log 2 scale.

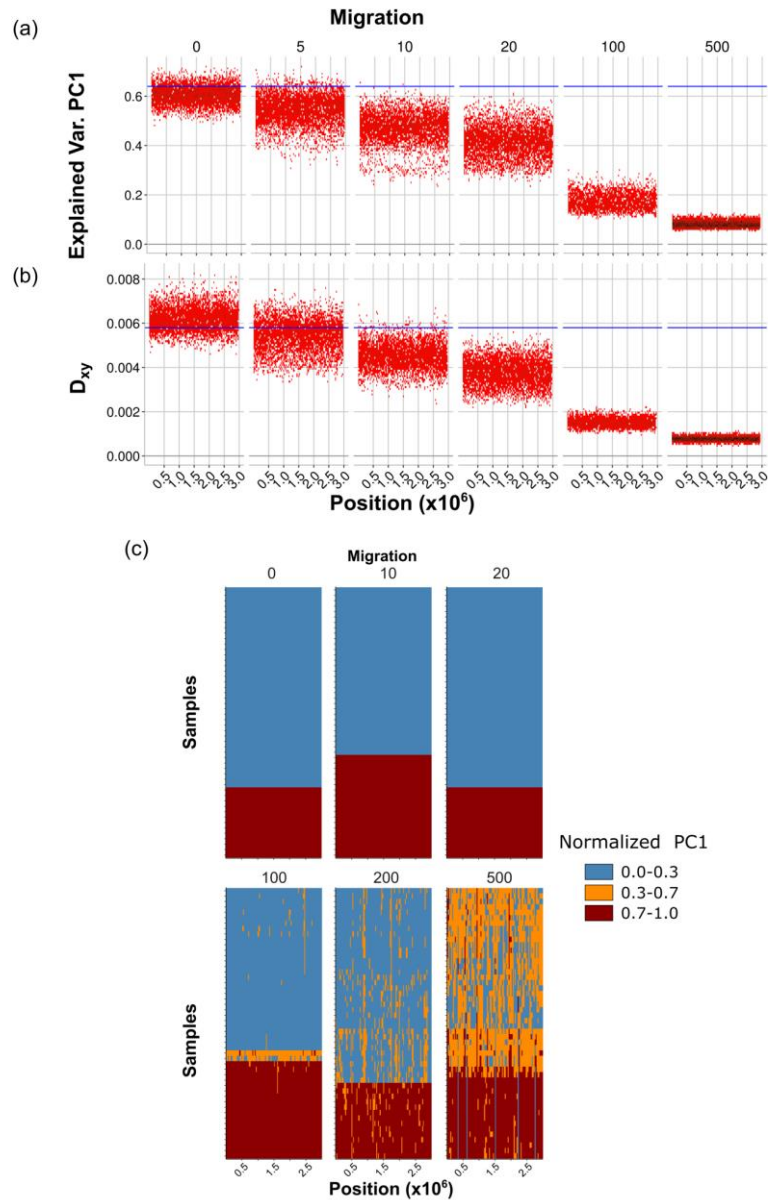


**Supplementary Figure 6: Distribution of ancestral *Sp* and *Sk* haplotypes along the genome.** Heatmap of ancestral *Sp* and *Sk* haplotypes along the genome for each sample. This figure corresponds to Figure 1c of the main manuscript, but uses all 161 samples.

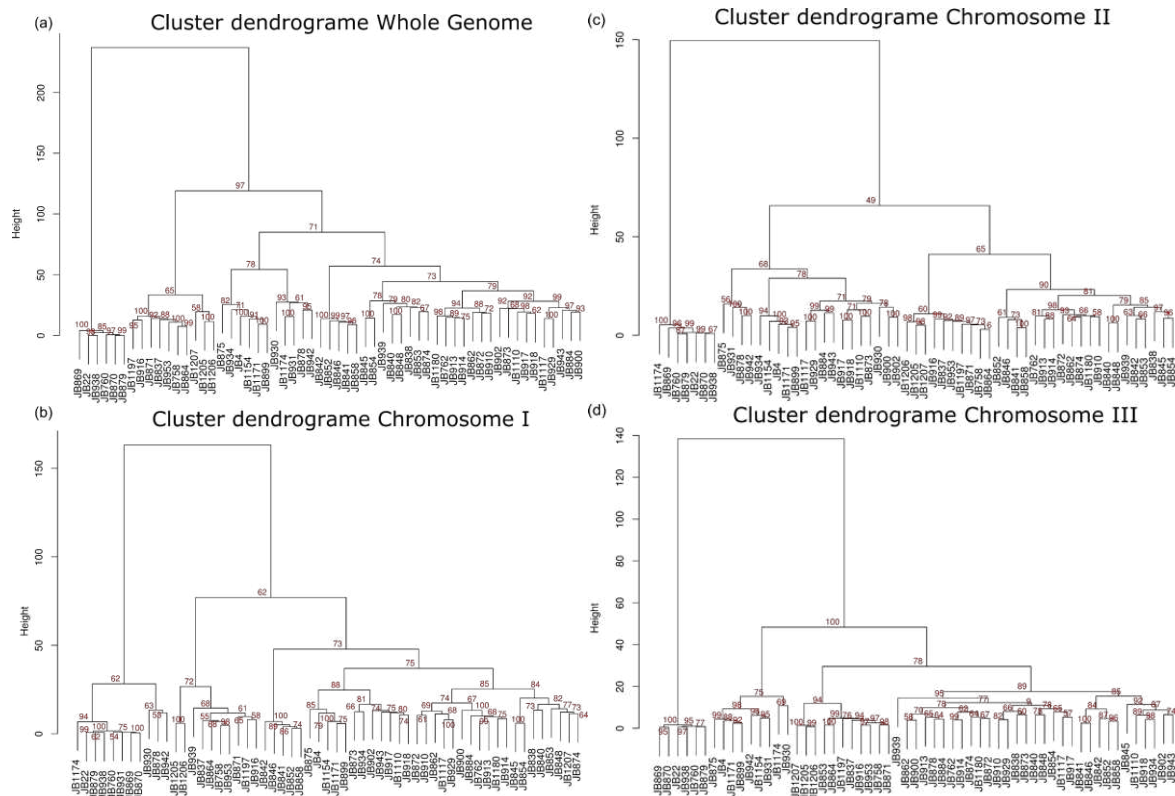


**Supplementary Figure 7: Individual based forward simulations of population divergence for a single genomic window.** Proportion of variance explained by PC1 over time (generations) (a-b) and divergence between subpopulations (Dxy in c-d), with different migration rates (in migrants per generation in a population of  $1 \cdot 10^6$ ). In all panels, the horizontal blue line corresponds to the observed empirical values. In a) and c) each line corresponds to the mean value from 100 simulations. Panels b) and d) are boxplots of all 100 simulations for migration rates below 20. These plots show that observed values are only achieved under migration rates below  $\sim 20$  migrants per generation.

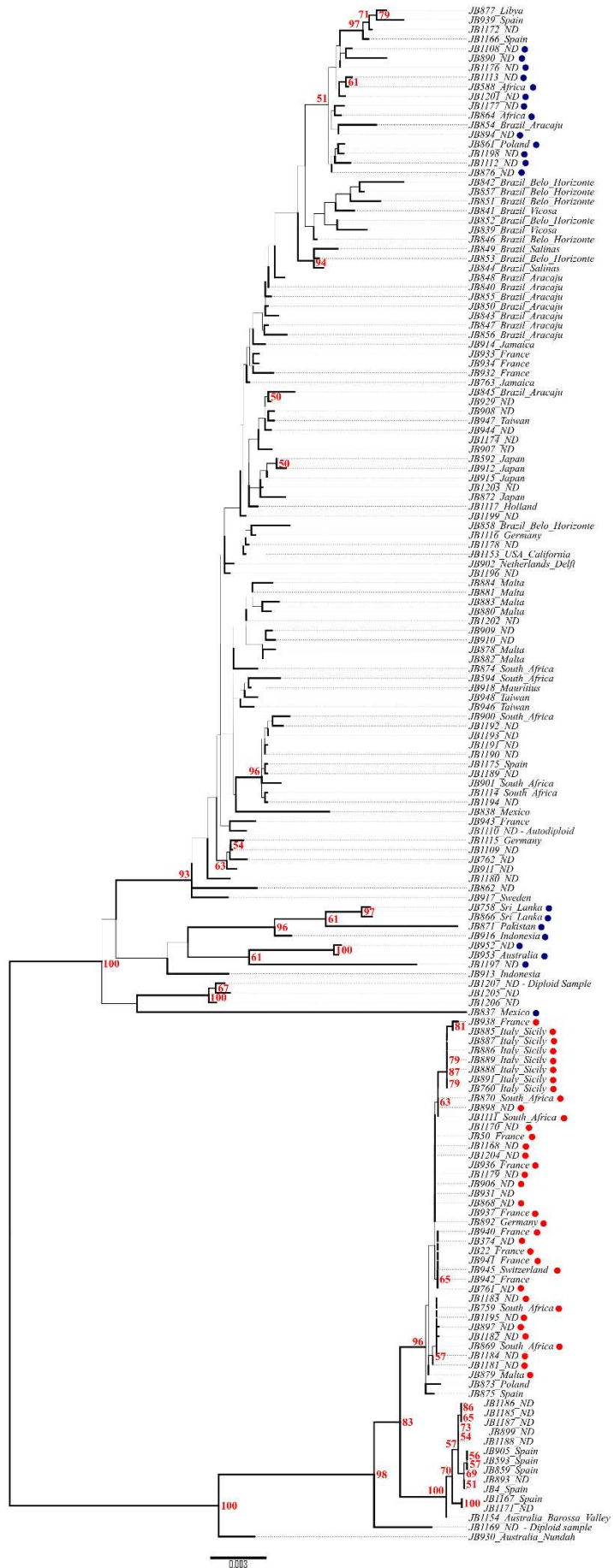




**Supplementary Figure 8: Individual base forward simulations for an entire chromosome with different levels of migration.** (a) Proportion of variance explained by PC1 and (b) divergence between subpopulations along simulated chromosomes of 3 Mb, after  $15 \cdot 10^6$  generations for 100 independent simulations. Different migration rates were used (in migrants per generation in a population of  $1 \cdot 10^6$ ). Horizontal blue lines correspond to observed empirical values. (c) A representative example simulation of the resulting genomes, divided into genomic windows and processed as empirical data to obtain a matrix as in Figure 1C. These plots show that the observed empirical values are only achieved under low migration rates (below  $\sim 20$  migrants per generation in (a) and (b)), but higher migration rate is needed to obtain large haplotype blocks with recombinated ancestral haplotypes as seen in the empirical data. Contrary to empirical data, the observed blocks under higher migration show low divergence ( $D_{xy}$  below 0.002) and no clear clustering of samples between subpopulations (high proportion of windows per sample with normalized PC1 between 0.3 and 0.7: yellow regions, contrary to observations in Supplementary Figures 1 - 3). General conclusions were consistent between replicated simulations.

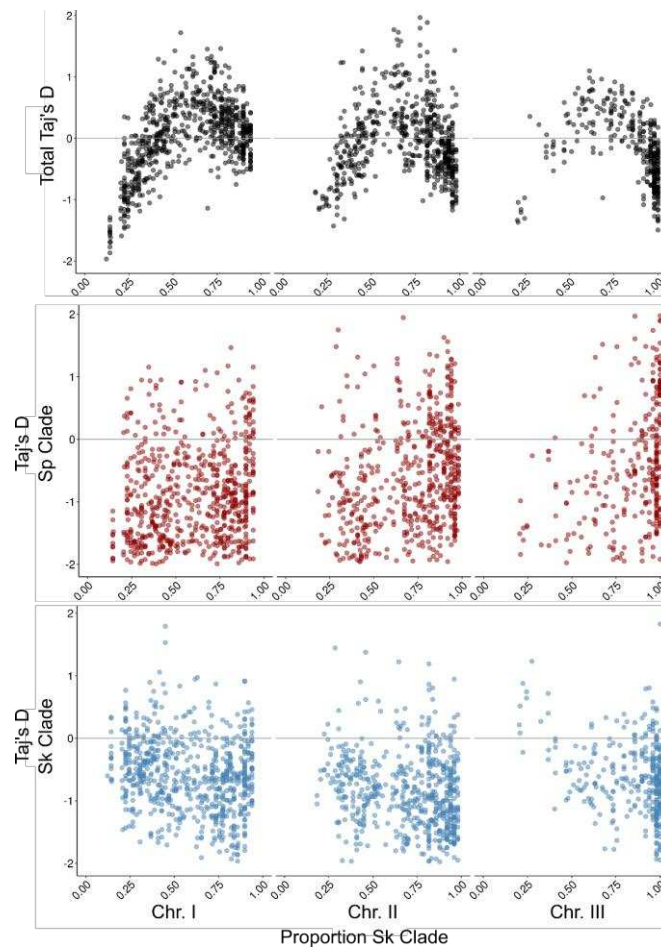


**Supplementary Figure 9: Clustering analyses by chromosome.** Clustering analyses using ancestral block distribution. Each panel shows the clustering using whole chromosome and independently by chromosome. Red numbers show bootstrapping support.

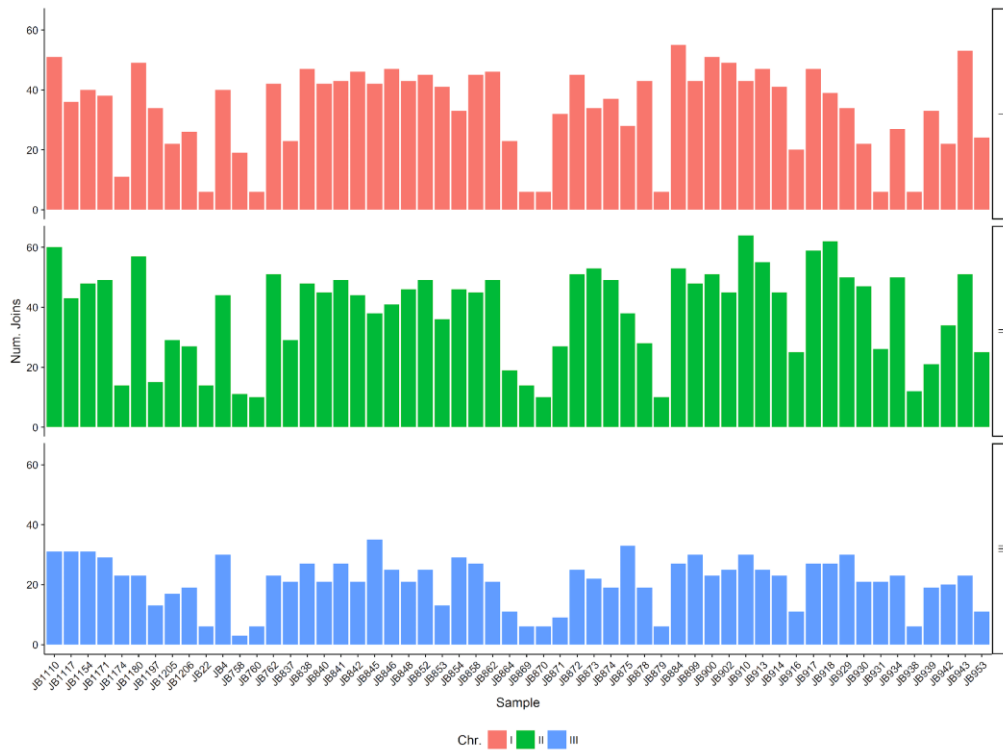


0.005

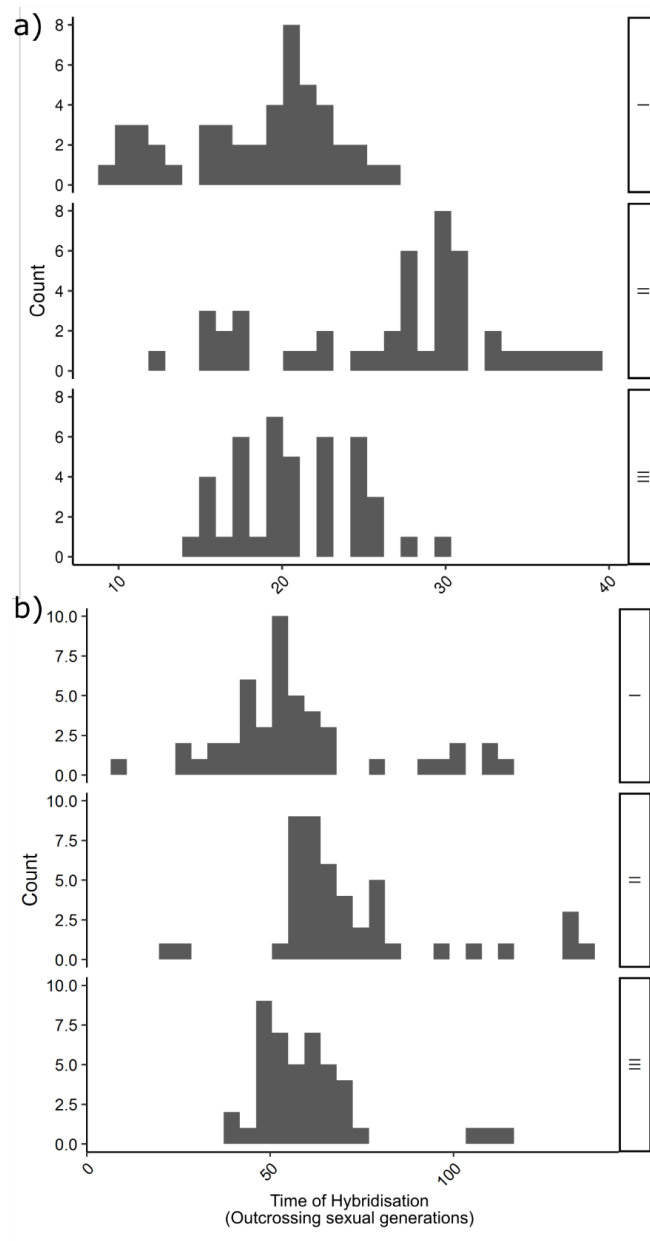
**Supplementary Figure 10: Mitochondrial phylogeny.** Unrooted maximum-likelihood tree for 161 samples based on mitochondrial SNPs. Red numbers show bootstrapping support when higher than 50. Tips show sample ID and sampling location as in Supplementary Table 1. Scale bar units in substitutions per site. Samples with high proportion from one ancestral population are indicated with dots (red: high *Sp* clade proportion, blue: high *Sk* clade proportion).



**Supplementary Figure 11: Tajima's D estimate.** Relationship between proportion of ancestral haplotypes (here represented by the proportion of *Sk* clade) and Tajima's D. Different panels show total Tajima's D using all samples (black dots) and samples from the *Sp* (red) or *Sk* (blue) clade only.



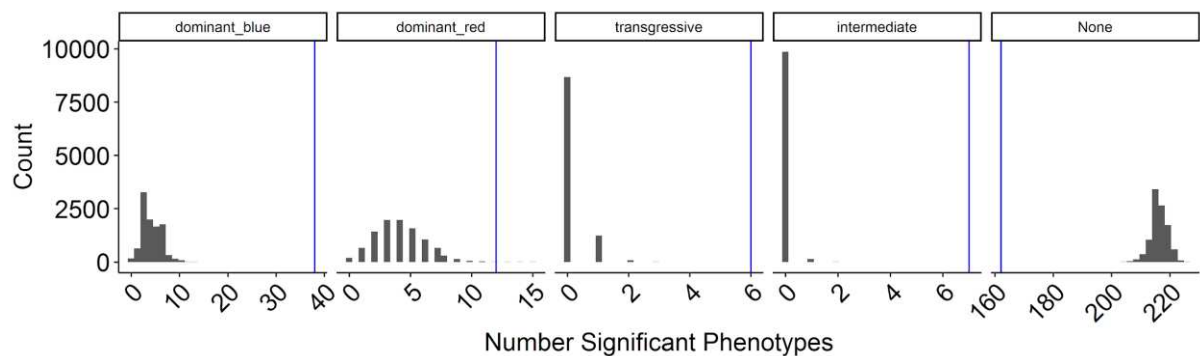
**Supplementary Figure 12: Number of transitions (joins) between *Sp* and *Sk* haplotypes along the genome per chromosome and sample.**



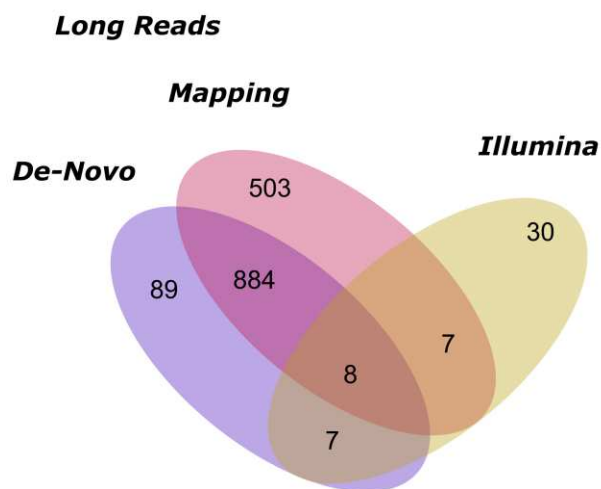
**Supplementary Figure 13: Estimated number of sexual generations since hybridisation.** Histogram displaying the number of outcrossing sexual generations since hybridisation using the model by Janzen *et al.* (2018). The analysis was divided by chromosome and sample. Counts represent the number of samples for which a given time of hybridization was inferred. The analysis was conducted using 200 and 50 SNPs per windows ((a) and (b) respectively).



**Supplementary Figure 14: Phenotypic distribution per trait.** Boxplot of phenotypic distribution using normalised values. Traits are divided by ancestral admixture proportions: pure *Sk* clade (blue), pure *Sp* clade (red) and hybrids (gray).

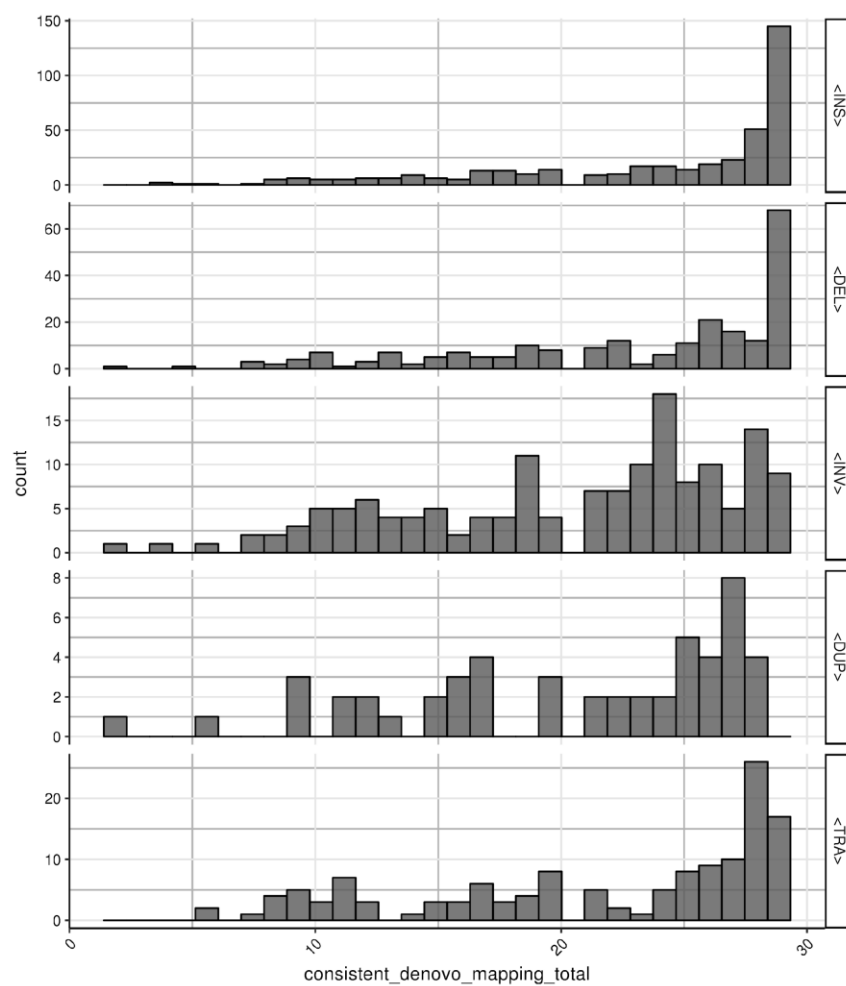


**Supplementary Figure 15: Permutation test with phenotypic data.** Histogram of total number of significant traits after randomising sample category (pure *Sp* clade, pure *Sk* clade and hybrids) without replacement. Blue lines show the observed number of significant traits. Matrix data was randomised 10000 times to produce the distribution per category group.

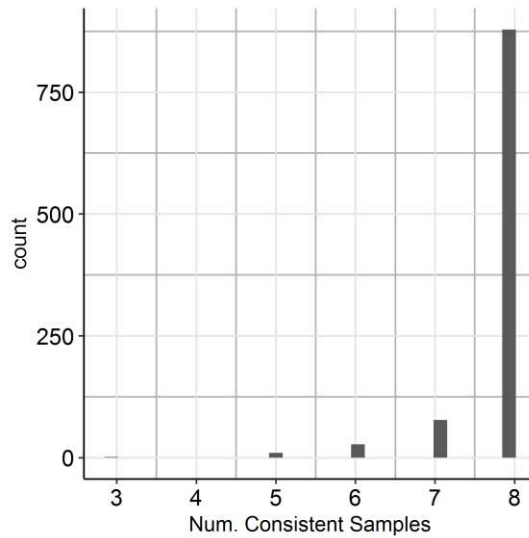


**Supplementary Figure 16: Total number of structural variant calls.** Venn diagram comparing the total number of structural variants in the reported list from Illumina reads (Jeffares, 2017), and long reads (this study). The latter is further subset by the two genotype calling approaches: *de-novo* and mapping reads.

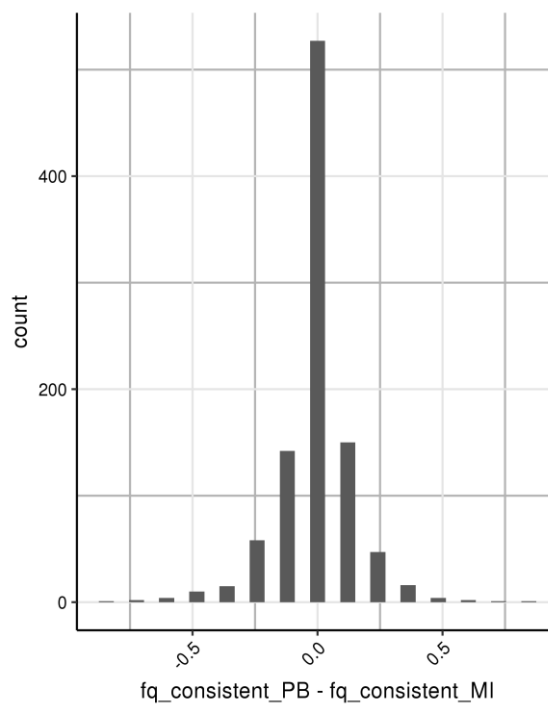




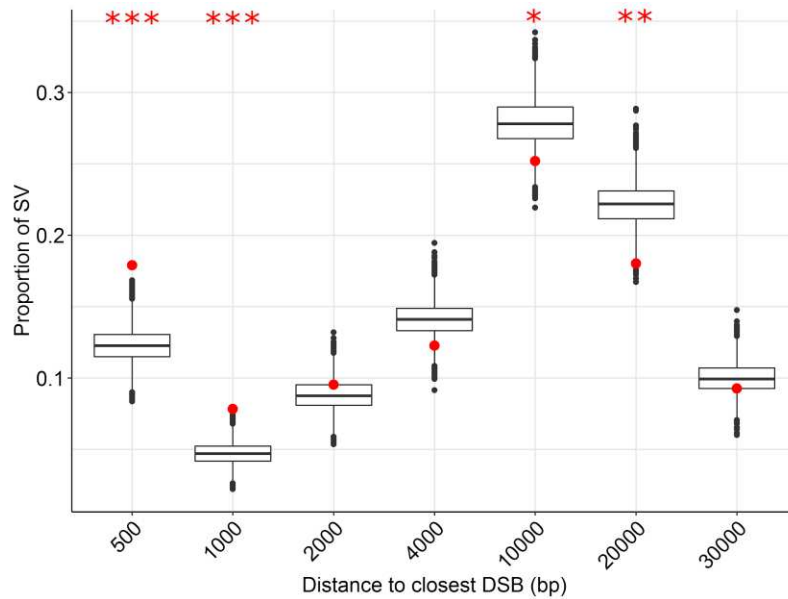
**Supplementary Figure 17: Comparison between SV detection using the de-novo vs. mapping approach.** Histogram of consistent genotypes of SVs in samples sequenced with PacBio and/or Nanopore (29 in total). Panels represent different types of SV (INS: insertion, DEL: deletion, INV: inversion, DUP: duplication, TRA: translocation). The obtained genotype from the de-novo and mapping approach in each sample and variant was compared. The histogram shows the number of variants with consistent mapping and de-novo genotype (no necessarily the same genotype between samples). For example, there are around 150 insertions with consistent mapping and de-novo genotype in all 29 samples. In another 50 insertion one sample out of the total shows different genotype between the mapping and de-novo approach.



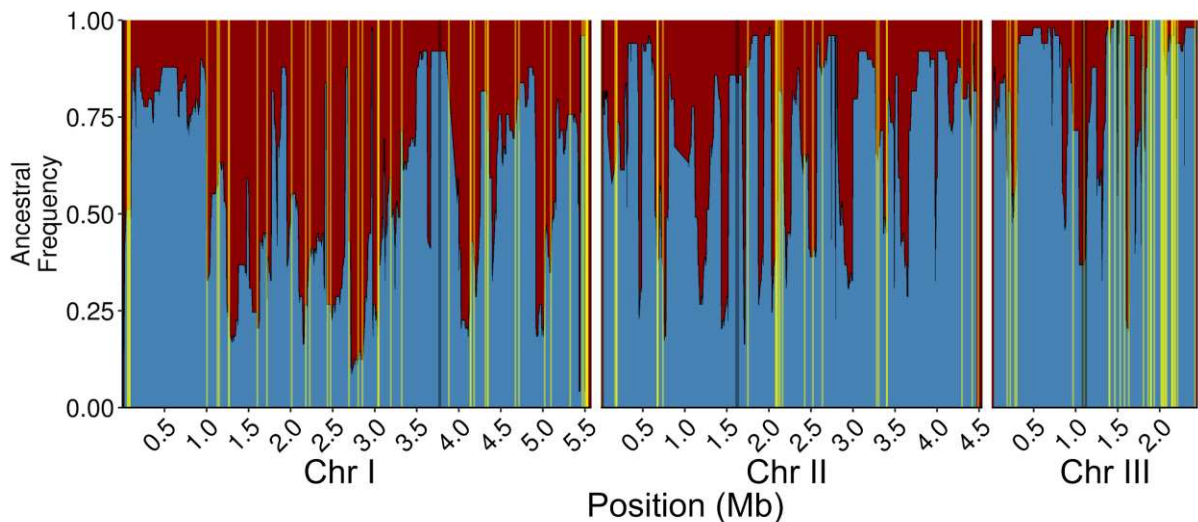
**Supplementary Figure 18: Consistency of SV genotype detection using PacBio vs. MinIon data.** Histogram of consistent genotypes of SVs in samples sequenced with both PacBio and Nanopore (8 strains in total). For each variants the genotype between the PacBio and Nanopore data was compared in each sample. The histogram shows the number of variants with up to 8 consistent samples. For example, 878 SVs show the same genotype per sample between PacBio and Nanopore data (not necessarily the same genotype between samples).



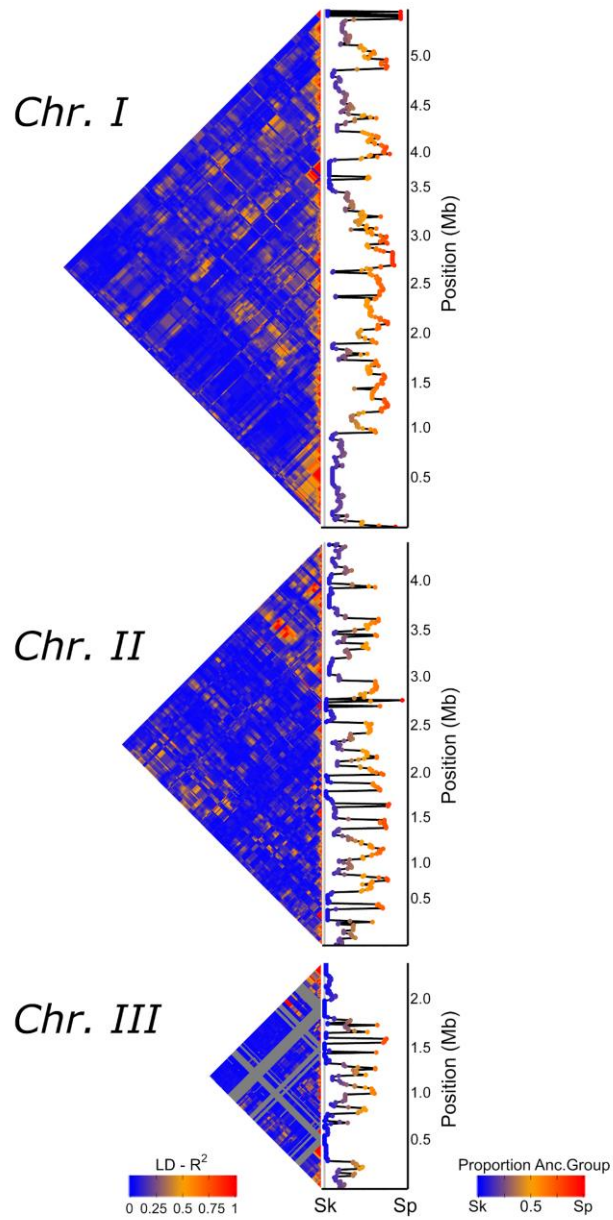
**Supplementary Figure 19: Difference in allele frequency using PacBio vs. MinIon data.** Histogram of the difference in observed allele frequency of samples sequenced with both PacBio and Nanopore (8 in total).



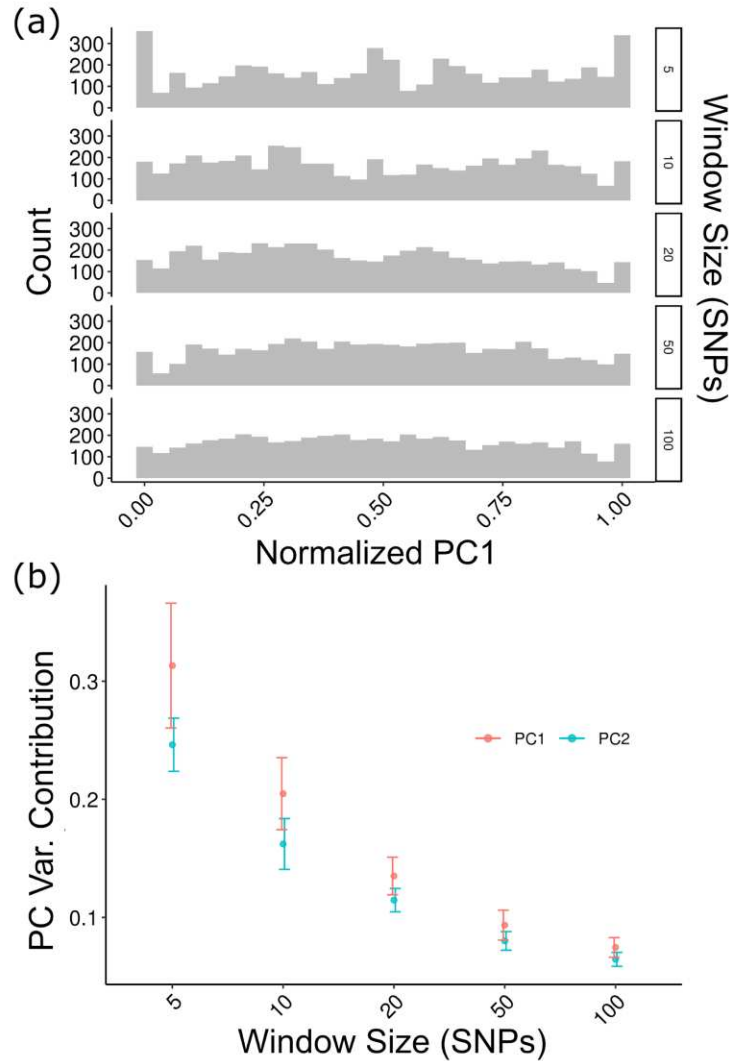
**Supplementary Figure 20: Boxplot displaying the proportion of SV relative to the physical genetic distance from the closest double-strand break.** Boxplot with the distribution of the expected proportion of structural variants by random permutation within different genetic distances. SV observed within 500bp and 1kb of the closest DSB are significantly overrepresented and those at 10kb or 20kb are underrepresented. Red points represent the observed proportions from long read sequencing data. Significance in difference between permutations and observed values are shown with asterisks: \* p-value < 0.05, \*\* p-value < 0.001, \*\*\* p-value < 0.0001.



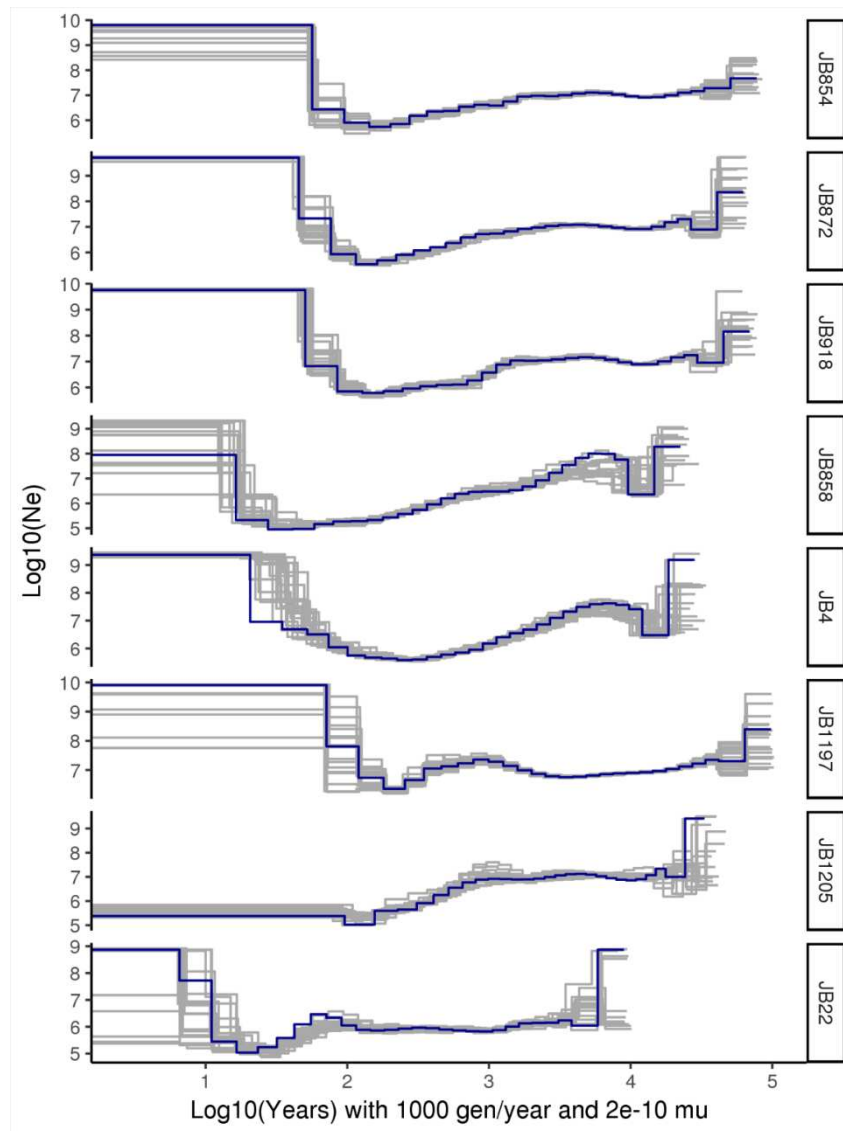
**Supplementary Figure 21: Distribution of divergent SV.** Proportion of *Sp* (red) and *Sk* (blue) ancestry across all 57 samples along the genome. Divergent between ancestral groups SV (with frequency difference > 0.7 between *Sp* and *Sk*) are shown with yellow lines. Centromeric regions are shown in gray.



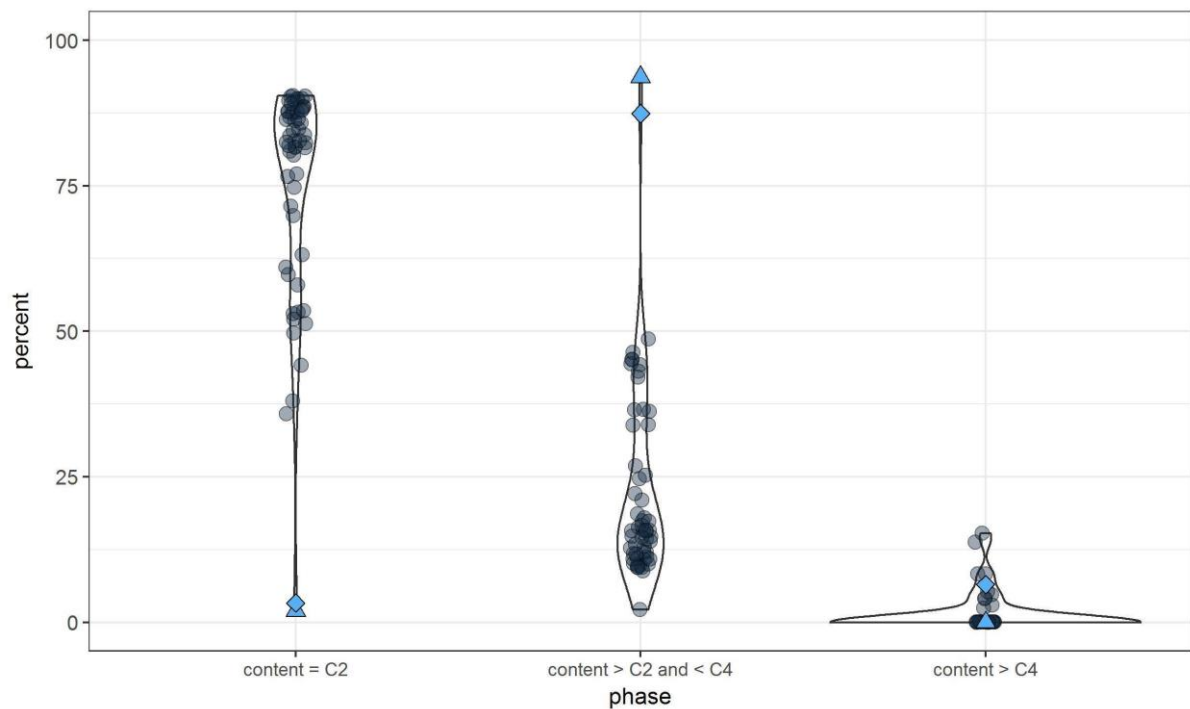
**Supplementary Figure 22: Linkage disequilibrium between pairs of genomic windows polarized by ancestry.** Heat map of linkage disequilibrium ( $R^2$ ) for all comparison between genomic windows (left panel). Proportions of ancestral groups ( $Sp$  or  $Sk$ ) along the genome are shown in the right panel. Genomic regions fixed for one of the ancestral groups are shown in gray areas in the heat map.



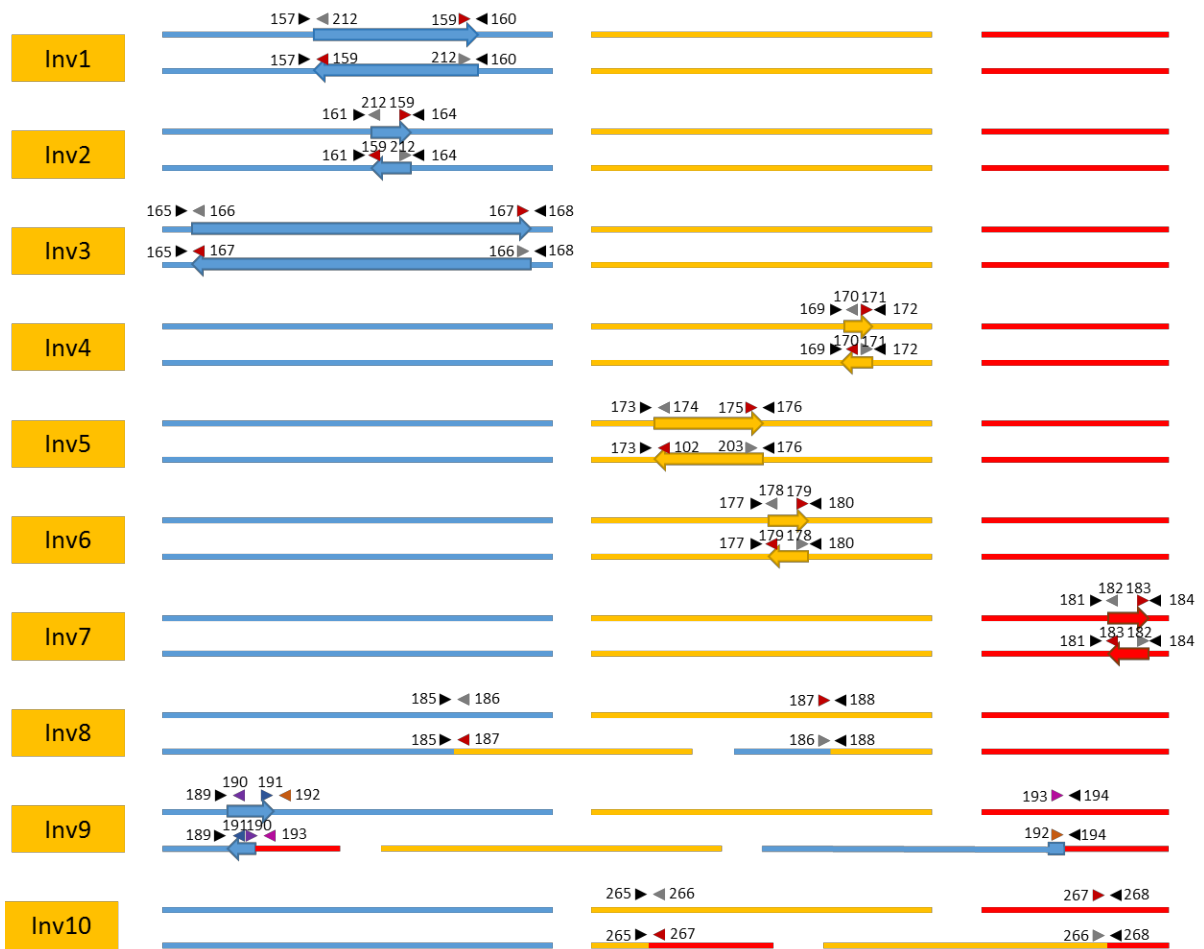
**Supplementary Figure 23: Individual based forward simulations for a single genomic window of different sizes.** a) Distribution of samples in the normalised PC1 for 100 replicate simulations, using window sizes from 5 to 100 SNPs. An increased number of counts for extreme values (1 and 0) are only observed in small windows (5 SNPs). This contrasts with empirical observations using window sizes of 200 SNPs where the values are almost exclusively centred around 0 and 1 (Supplementary Figure 2). b) Proportion of variance explained by PC1 and PC2 in the PCA using different window sizes. Simulations using as few as 5 SNPs per window could artificially divide a panmictic population into two clusters and explain 40 % of the variance in PC1. However, the inclusion of more SNPs per window, reduced erroneous clustering and reduced the variance to  $\ll 0.1$  for 100 SNPs. None of the simulations (100 replicates per window size) approached the empirical value of 64 % of the variance explained by PC1 using a window size of 200 SNPs providing evidence that bimodal group structure was not an artefact of small window size.



**Supplementary Figure 24: Inferred effective population size over time with multiple sequentially Markovian coalescence analyses (MSMC).** Analysis was divided by secondary clusters presented in Figure 1c. Each cluster is label with one representative of the cluster. Inferred values are shown with the blue line and bootstraps with grey lines. Time in x axis in log10 scale using 1000 generations per year and mutation rate of  $2 \times 10^{-10}$ . Present time is in  $x=0$  and increase in the past. Effective population size in log10 scale.

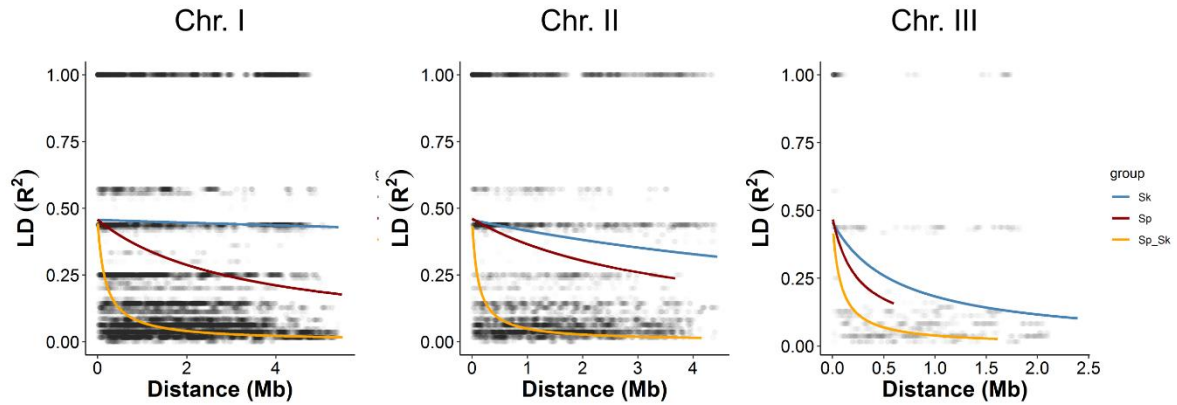


**Supplementary figure 25: DNA content per strain.** Representation of flow cytometry measurements of percentage of cells with nuclear DNA content  $< C2$  (two times haploid genomic content; left), nuclear content between  $C2$  and  $C4$  (middle) and larger than  $C4$  (right). Due to the short G1 phase and late cytokinesis, few cells with  $C1$  content are found in fission yeast. Haploid cells are thus mostly found in the  $C2$  phase. Diploid cells will be mostly in  $C4$  or larger. The strain with high heterozygosity (JB1207) is indicated by the blue diamond and it has a large proportion of cells with large genomic content. Additionally, strain JB1169 (blue triangle) appears to be of higher ploidy, though it does not show increased heterozygosity, which suggests this strain was formed by auto-diploidization. Data from Jeffares et al. 2015.



**Supplementary Figure 26: Overview of PCR primers used to verify inversions and translocations.** For each SV first the positions in the reference genome are given (top), and below the organization in the rearranged form as observed in the long-read *de novo* assemblies. The three lines represent Chromosomes I, II and III. The small arrows indicate the position and direction of the primers with the numbers of the primers indicated. The large arrows indicate the size and orientation of inversions. Note that more than one SV can occur per strain, and that the representations are thus not always representations of actual strains. Primers in ‘Inv10’ from Zanders et al. 2014.





**Supplementary figure 27: Example of decay in linkage disequilibrium (LD) with genetic distance using one representative per cluster.** Relationship between LD ( $R^2$ ) and physical distance is depicted for each chromosome. Black points represent values for each window pair comparison. Lines show non-linear regression model based on Hill & Weir (1988) and Remington et al. (2001). LD estimates were divided into three categories representing comparison between windows of shared ancestry (Sp-Sp or Sk-Sk) reflecting positive ancestry disequilibrium (AD) or of opposite ancestry (Sk-Sp) reflecting negative AD.